
**1 Local wind regime induced by giant linear dunes:
2 comparison of ERA5-Land re-analysis with surface
3 measurements**

**4 Cyril Gadal · Pauline Delorme ·
5 Clément Narteau · Giles F.S. Wiggs ·
6 Matthew Baddock · Joanna M. Nield ·
7 Philippe Claudin**

8
9 Received: DD Month YEAR / Accepted: DD Month YEAR

10 Abstract

11 Emergence and growth of sand dunes results from the dynamic interaction be-
12 tween topography, wind flow and sediment transport. While feedbacks between
13 these variables are well studied at the scale of a single dune, the average effect
14 of a periodic dune pattern on atmospheric flows remains poorly constrained
15 due to a lack of data in major sand seas. Here, we compare field measurements
16 of surface wind data to the predictions of the ERA5-Land climate reanalysis at
17 four locations in Namibia, including within the giant-dune field of the Namib
18 sand sea. In the desert plains to the north of the sand sea, observations and
19 predictions agree well. This is also the case in the interdune areas of the sand
20 sea, except for the weak winds blowing at night, which exhibit additional com-
21 ponents aligned with the giant dune orientation, which are not predicted by
22 the ERA5-Land reanalysis. We quantify these similarities and differences and

C. Gadal

Institut de Mécanique des Fluides de Toulouse, Université de Toulouse Paul Sabatier, CNRS,
Toulouse INP-ENSEEIHT, Toulouse, France. E-mail: cyril.gadal@imft.fr

P. Delorme

Energy and Environment Institute, University of Hull, Hull, UK.

C. Narteau

Institut de Physique du Globe de Paris, Université de Paris, CNRS, Paris, France.

G. Wiggs

School of Geography and the Environment, University of Oxford, Oxford, UK.

M. Baddock

Geography and Environment, Loughborough University, Loughborough, UK.

J.M. Nield

School of Geography and Environmental Science, University of Southampton, Southampton,
UK.

P. Claudin

Physique et Mécanique des Milieux Hétérogènes, CNRS, ESPCI Paris, PSL Research Uni-
versity, Université de Paris, Sorbonne Université, Paris, France.

23 provide a physical understanding of the relevant aerodynamical regimes to
24 relate them to the daily cycle of the turbulent atmospheric boundary layer
25 over a dune pattern of given wavelength. We conclude by identifying the con-
26 ditions under which the ERA5-Land reanalysis data can reliably be used to
27 study dune morphodynamics. We also propose that, in multidirectional wind
28 regimes, deflections of specific winds by giant dunes could explain the occur-
29 rence of secondary dune patterns with a different orientation to the primary
30 structures between which they develop.

31 **Keywords** Atmospheric boundary layer · Sand dunes · Fluid-structure
32 interactions

33 1 Introduction

34 The description of turbulent flows over complex topography is relevant for a
35 large variety of different environmental systems (Finnigan et al. 2020). For
36 example, the flow over hills is of primary interest for wind power, meteorolog-
37 ical and air pollution phenomena (Taylor et al. 1987). The properties of
38 these flows are also key to the understanding of geophysical phenomena, in-
39 cluding the formation of wind-driven waves on the ocean surface (Sullivan and
40 McWilliams 2010), dissolution bedforms (Claudin et al. 2017), or sedimentary
41 ripples and dunes (Charru et al. 2013; Courrech du Pont 2015). Importantly,
42 the troposphere presents a vertical structure, with a lower convective bound-
43 ary layer, of typical kilometer-scale thickness, capped by a stably stratified
44 region (Stull 1988). The largest topographic obstacles, such as mountains, can
45 therefore interact with this upper region and lead to internal wave generation
46 or significant wind disturbances, such as lee-side downslope winds (Durran
47 1990).

48 Focusing on the wind close to the surface, two related topographic feed-
49 backs on the windflow over dunes can be commented on separately. First is
50 the effect on wind speed, with documented flow acceleration on upwind slopes
51 (Weaver and Wiggs 2011) and deceleration on downwind slopes (Baddock et al.
52 2007), where the speed-up factor is essentially proportional to the obstacle as-
53 pect ratio (Jackson and Hunt 1975). Importantly, the velocity maximum is
54 typically shifted upwind of the obstacle crest. This behaviour has been the-
55oretically predicted by means of asymptotic analysis of a neutrally stratified
56 boundary-layer flow over an obstacle of vanishing aspect ratio (Jackson and
57 Hunt 1975; Mason and Sykes 1979; Sykes 1980; Hunt et al. 1988; Belcher and
58 J.C.R. 1998). Experiments in flumes (Zilker et al. 1977; Zilker and Hanratty
59 1979; Frederick and Hanratty 1988; Poggi et al. 2007; Bristow et al. 2022),
60 in wind tunnels (Gong and Ibbetson 1989; Finnigan et al. 1990; Gong et al.
61 1996) and in field conditions (Taylor and Teunissen 1987; Claudin et al. 2013;
62 Fernando et al. 2019; Lü et al. 2021), have also documented this effect. In-
63 terestingly, a similar behaviour exists for the pressure perturbation, but with
64 a slight downwind shift for the pressure minimum (Claudin et al. 2021). The
65 second effect, much less studied, is the flow deflection that occurs when the
66 incident wind direction is not perpendicular to the ridge crest. While predicted
67 to be small (less than 10°) in the linear regime valid for shallow topography
68 (Gadal et al. 2019), significant flow steering has been reported in the field on
69 the downwind side of steep enough obstacles, such as mountain ranges (Kim
70 et al. 2000; Lewis et al. 2008; Fernando et al. 2019), well-developed sand dunes
71 (Walker et al. 2009; Hesp et al. 2015; Walker et al. 2017; Smith et al. 2017; de
72 Winter et al. 2020), and valley topographies (Wiggs et al. 2002; Garvey et al.
73 2005).

74 For practical reasons, wind measurement over sand dunes has been per-
75 formed over small bedforms, typically a few meters high (corresponding to
76 tens of meters long) (e.g. Lancaster et al. (1996), Mckenna Neuman et al.
77 (1997), Sauermann et al. (2003), Andreotti et al. (2002), Walker and Nick-

ling (2002), Weaver and Wiggs (2011)). Giant dunes, with kilometer-scale wavelengths and heights of tens of meters, are more difficult to investigate although for several reasons they provide a choice configuration for the study of turbulent flows over a complex topography. First, one expects larger wind disturbances for larger obstacles. Secondly, their large size makes them interact with the vertical structure of the atmosphere (Andreotti et al. 2009). Third, they usually form large patterns in sand seas and thus behave as rather clean periodic perturbations, in contrast with isolated dunes. Finally, because the morphodynamics of aeolian bedforms are strongly dependent on the local wind regime (Livingstone and Warren 2019), one can expect to see the consequences of windflow disturbance by large dunes on neighbouring small dunes. A similar effect is observed on the properties of impact ripple patterns due to the presence of dunes (Howard 1977; Hood et al. 2021).

Atmospheric flows have been much studied at the desert-scale with climate reanalyses based on global atmospheric models (Blumberg and Greeley 1996; Livingstone et al. 2010; Ashkenazy et al. 2012; Jolivet et al. 2021; Hu et al. 2021), such as ERA-40, ERA-Interim or ERA-5 (Uppala et al. 2005; Dee et al. 2011; Hersbach et al. 2020). However, the spatial resolution (tens of kilometers) of these reanalyses implies average quantities that do not resolve the smaller scales of interest, which range from individual dunes to small mountains (Livingstone et al. 2010). Recently, the release of ERA5-Land has resolved this limitation by providing up to 70 years of hourly wind predictions at a 9 km spatial resolution (Muñoz-Sabater et al. 2021). However, its validity remains to be studied, especially in remote desert areas where assimilation of measured data is very low.

In this work, we compare local wind speeds and directions measured by meteorological stations at four different locations inside and north of the giant-dune field of the Namib sand sea to the regional predictions of the ERA5-Land climate reanalysis. Where the meteorological stations are surrounded by a relatively flat environment, we show that local measurements and regional predictions agree well. The agreement is also good in the interdune areas of the sand sea, except for some weak winds blowing at night, which exhibit an additional component aligned with the giant dune orientation. These winds are not predicted by the ERA5-Land reanalysis (section 2). Further, we are able to link the magnitude of these differences to the circadian cycle of the atmospheric boundary layer (section 3). Finally, we draw implications for the wind disturbances on smaller-scale dunes (section 4), suggesting a possible origin for crossing dunes.

116 2 Wind regimes across the Namib Sand Sea

117 We measured the wind regime at four different locations in Namibia, representative of various arid environments across the Namib desert (Fig. 1, Online
118 Resource Fig. S1). The Etosha West station was located at the Adamax wa-
119 terhole to the west of Etosha Pan in northern Namibia, in a sparsely vegetated

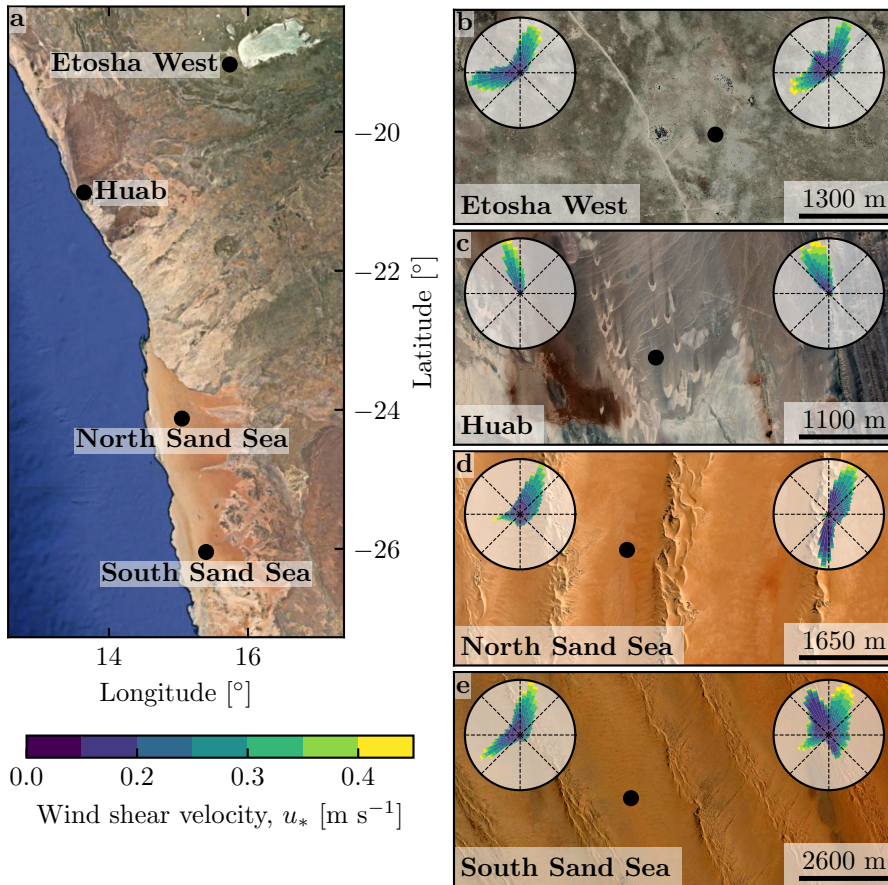


Fig. 1 Wind data used in this study **a:** Location of the different sites in Namibia. **b–e:** Satellite images of these different environments (Google-Earth, Maxar Technologies, CNES/Airbus). In each subplot, the left and right wind roses represent the data from the ERA5-Land climate reanalysis and the local wind stations, respectively. Note that the bars show the direction towards which the wind blows. The black dots show the location of local wind stations.

area. The Huab station was near the coast on a hyper-arid flat gravel plain lying north the ephemeral Huab river. Here, barchan dunes up to a few meters in height develop from the sediment blowing out of the river valley (Nield et al. 2017; Hesp and Hastings 1998). These two stations were both located in relatively flat environments. In contrast, the North Sand Sea and South Sand Sea stations were located in the interdunes between linear dunes with kilometer-scale wavelengths, hectometer-scale heights and superimposed patterns. In this section, we describe and compare winds from local measurements and climate reanalysis predictions.

130 2.1 Wind and elevation data

131 At each meteorological station (Fig. 1), wind speed and direction were sampled
132 every 10 minutes using cup anemometers (Vector Instruments A100-LK) and
133 wind vanes (Vector Instruments W200-P) at heights which varied between 2 m
134 and 3 m depending on the station. The available period of measurements at
135 each station ranged from 1 to 5 discontinuous years distributed between 2012
136 and 2020 (Online Resource Fig. S2). We checked that at least one complete
137 seasonal cycle was available for each station. Regional winds were extracted
138 at the same locations and periods from the ERA5-Land dataset, which is a
139 replay at a smaller spatial resolution of ERA5, the latest climate reanalysis
140 from the ECMWF (Hersbach et al. 2020; Muñoz-Sabater et al. 2021). This
141 dataset provided hourly predictions of the 10-m wind velocity and direction
142 at a spatial resolution of $0.1^\circ \times 0.1^\circ$ (≈ 9 km in Namibia).

143 To enable direct comparison, the local wind measurements were averaged
144 into 1-hr bins centered on the temporal scale of the ERA5-Land estimates
145 (Online Resource Fig. S3). As the wind velocities of both datasets were pro-
146 vided at different heights, we converted them into shear velocities u_* (Online
147 Resource section 1), characteristic of the turbulent wind profile. Wind roses
148 in Fig. 1(b–e) show the resulting wind data.

149 Dune properties were computed using autocorrelation on the 30-m Digital
150 Elevation Models (DEMs) of the shuttle radar topography mission (Farr et al.
151 2007). For the North and South Sand Sea stations, we obtain, respectively,
152 orientations of 85° and 125° with respect to the North, wavelengths of 2.6 km
153 and 2.3 km and amplitudes (or half-heights) of 45 m and 20 m (Online Resource
154 Fig. S5 for more details). This agrees with direct measurements made on site.

155 2.2 Comparison of local and regional winds

156 The measured and predicted wind regimes are shown in Fig. 1. In the Namib,
157 the regional wind patterns are essentially controlled by the sea breeze, result-
158 ing in strong northward components (sometimes slightly deviated by the large
159 scale topography) present in all regional wind roses (Lancaster 1985). These
160 daytime winds are dominant during the period October-March (Fig. 2f and
161 Online Resource Fig. S6f). During April-September, an additional (and often
162 nocturnal) easterly component can also be recorded, induced by the combina-
163 tion of katabatic winds forming in the mountains, and infrequent ‘berg’ winds,
164 which are responsible for the high wind velocities observed (Lancaster et al.
165 1984). The frequency of these easterly components decreases from inland to
166 the coast. As a result, bidirectional wind regimes within the Namib Sand Sea
167 and at the west Etosha site (Fig. 1b,d,e) and a unidirectional wind regime on
168 the coast at the outlet of the Huab River (Fig. 1c) are observed.

169 In the case of the Etosha West and Huab stations, the time series of wind
170 speed and direction from the regional predictions quantitatively match those
171 corresponding to the local measurements (Fig. 2a–d) and Online Resource

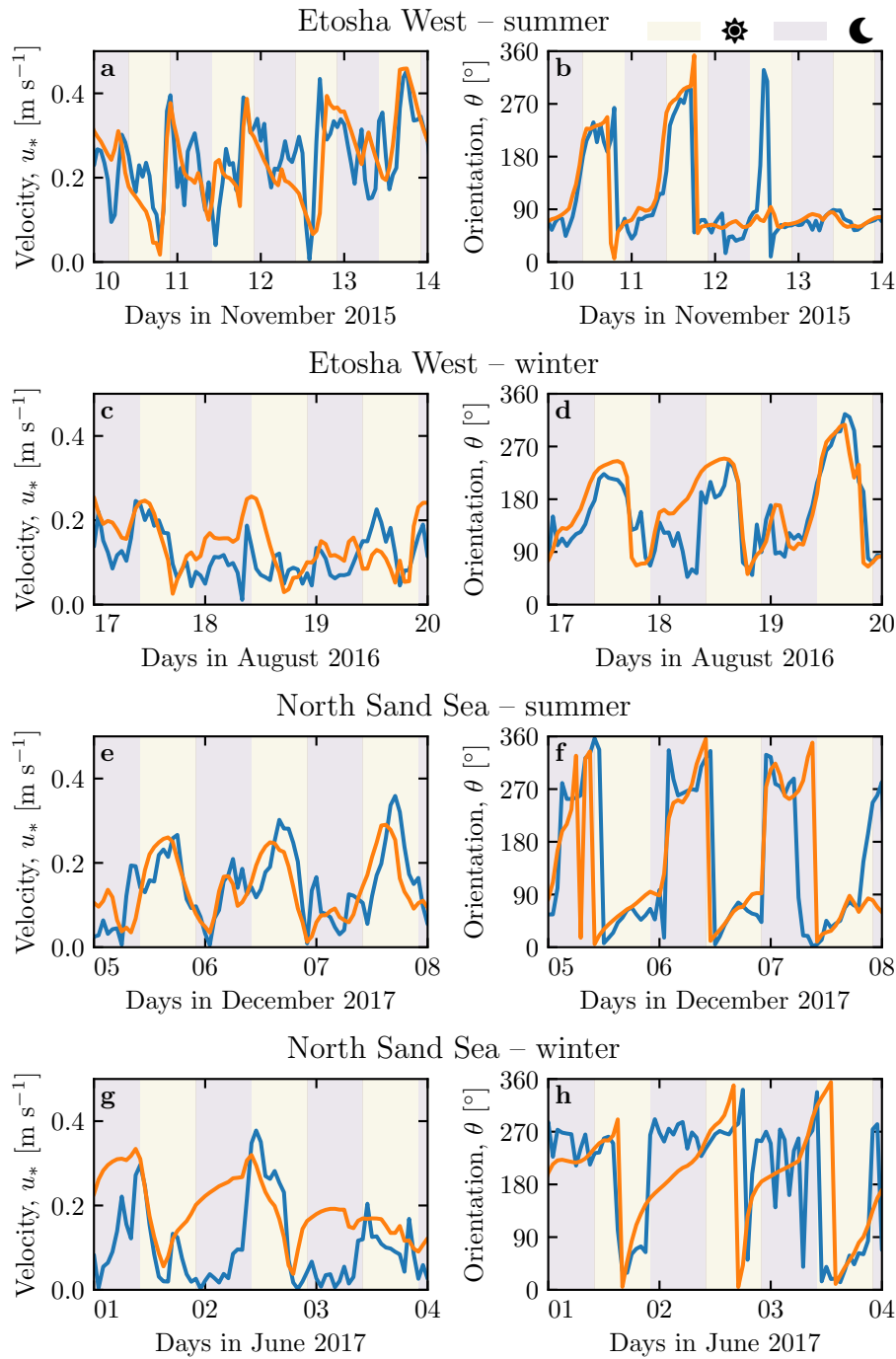


Fig. 2 Temporal comparison between the wind data coming from the ERA5-Land climate reanalysis (orange lines) and from the local measurements (blue lines). Coloured swathes indicate day (between 1000 UTC and 2200 UTC) and night (before 1000 UTC or after 2200 UTC). **a–b:** Etosha West station in summer. **b–c:** Etosha West station in winter. **d–e:** North Sand Sea station in summer. **f–g:** North Sand Sea station in winter. Time series of the two other stations are shown in Online Resource Fig. S6.

Figs. S6a–d, S7, S9). For the North Sand Sea and South Sand Sea stations within the giant dune field, we observe that this agreement is also good, but limited to the October–March time period (Fig. 2e–h and Online Resource Fig. S6e–h). However, the field-measured wind roses exhibit additional wind components aligned with the giant dune orientation, as evidenced on the satellite images (Fig. 1c,d).

More precisely, during the April–September period, the local and regional winds in the interdune match during daytime only, i.e. when the southerly/southwesterly sea breeze dominates (Figs. 2e,f and 3, Online Resource Fig. S8). In the late afternoon and during the night, when the easterly ‘berg’ and katabatic winds blow, measurements and predictions differ. In this case, the angular wind distribution of the local measurements exhibits two additional modes corresponding to reversing winds aligned with the giant dune orientation (purple frame in Fig. 3, Online Resource Figs. S8 and S10). This deviation is also associated with a general attenuation of the wind strength (Online Resource Fig. S11). Remarkably, all these figures show that these wind reorientation and attenuation processes occur only at low velocities of the regional wind, typically for $u_{*,\text{ERA}} \lesssim 0.2 \text{ m s}^{-1}$. For shear velocities larger than $u_{*,\text{ERA}} \simeq 0.3 \text{ m s}^{-1}$, the wind reorientation is not apparent. Finally, for intermediate shear velocities, both situations of wind flow reoriented along the dune crest and not reoriented can be successively observed (Online Resource Fig. S10). Importantly, these values are not precise thresholds, but indicative of a crossover between regimes, whose physical interpretation is discussed in the next section.

3 Influence of wind speed and circadian cycle on the atmospheric boundary layer

The wind deflection induced by linear dunes has previously been related to the incident angle between wind direction and crest orientation, with a maximum deflection evident for incident angles between 30° and 70° (Walker et al. 2009; Hesp et al. 2015). In the data analysed here, the most deflected wind at both the North and South Sand Sea stations is seen to be where the incident angle is perpendicular to the giant dunes (Figs. 1 and 3, Online Resource Fig. S8). It therefore appears that in our case, the incident wind angle is not the dominant control on maximum wind deflection. Further, and as shown in Fig. 3, winds of high and low velocities show contrasting behaviour in characteristics of deflection. This suggests a change in hydrodynamical regime between the winds. In this section, we discuss the relevant parameters associated with the dynamical mechanisms that govern the interactions between the atmospheric boundary layer flow and giant dune topographies. This analysis allows us to provide a physics-based interpretation of our measured wind data.

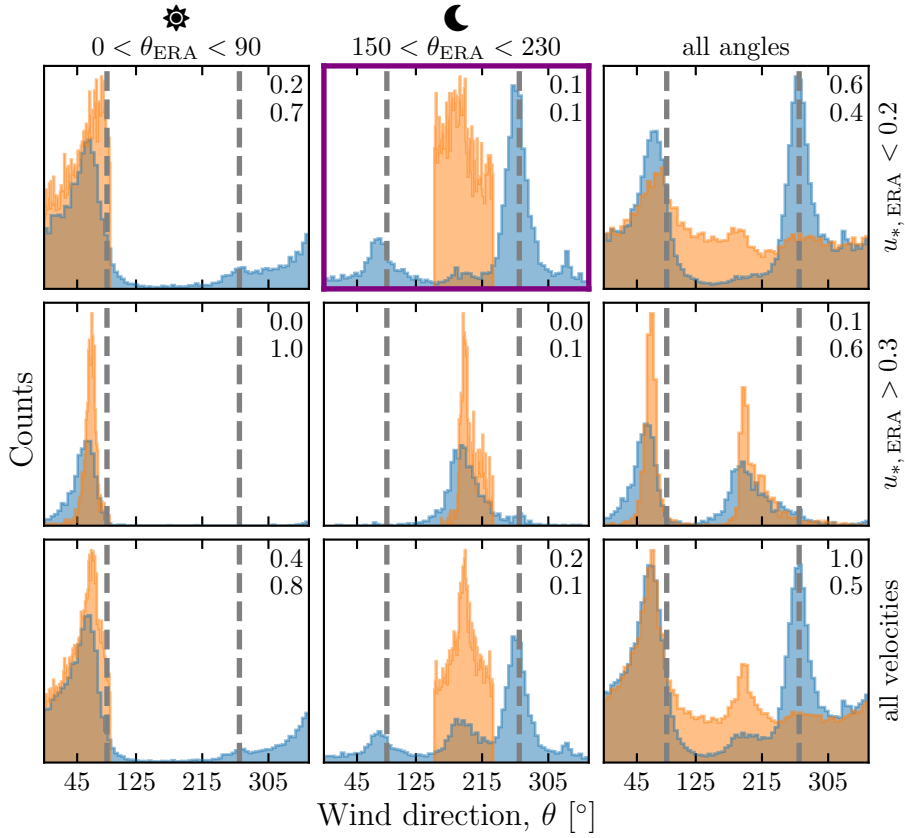


Fig. 3 Distributions of wind direction at the North Sand Sea Station for the ERA5-Land climate reanalysis (orange) and the local measurements (blue). In each subplot, both distributions are plotted from the same time steps, selected with constraints on the wind direction (columns) and/or wind velocity (rows) of the ERA5-Land dataset. The grey vertical dashed lines indicate the dune orientation. The numbers at the top right give the percentage of time steps selected in each sub-range, as well as the percentage corresponding to the daytime (between 1000 UTC and 2200 UTC). The purple frame highlights the regime (low wind velocities, nocturnal easterly wind) in which the data from both datasets differ. A similar figure can be obtained for the North Sand Sea station (Online Resource Fig. S8).

211 3.1 Flow over a modulated bed

212 Taking as a reference the turbulent flow over a flat bed, the general framework
 213 of our study is understanding and describing the flow response to a bed mod-
 214 ulation (e.g. a giant dune). Without loss of generality, we can consider in this
 215 context an idealised bed elevation in the form of parallel sinusoidal ridges, with
 216 wavelength λ (or wavenumber $k = 2\pi/\lambda$) and amplitude ξ_0 , and where the ref-
 217 erence flow direction makes a given incident angle with respect to the ridge
 218 crest (Andreotti et al. 2012). Part of this response, on which we focus here,
 219 is the flow deflection by the ridges. In a simplified way, it can be understood

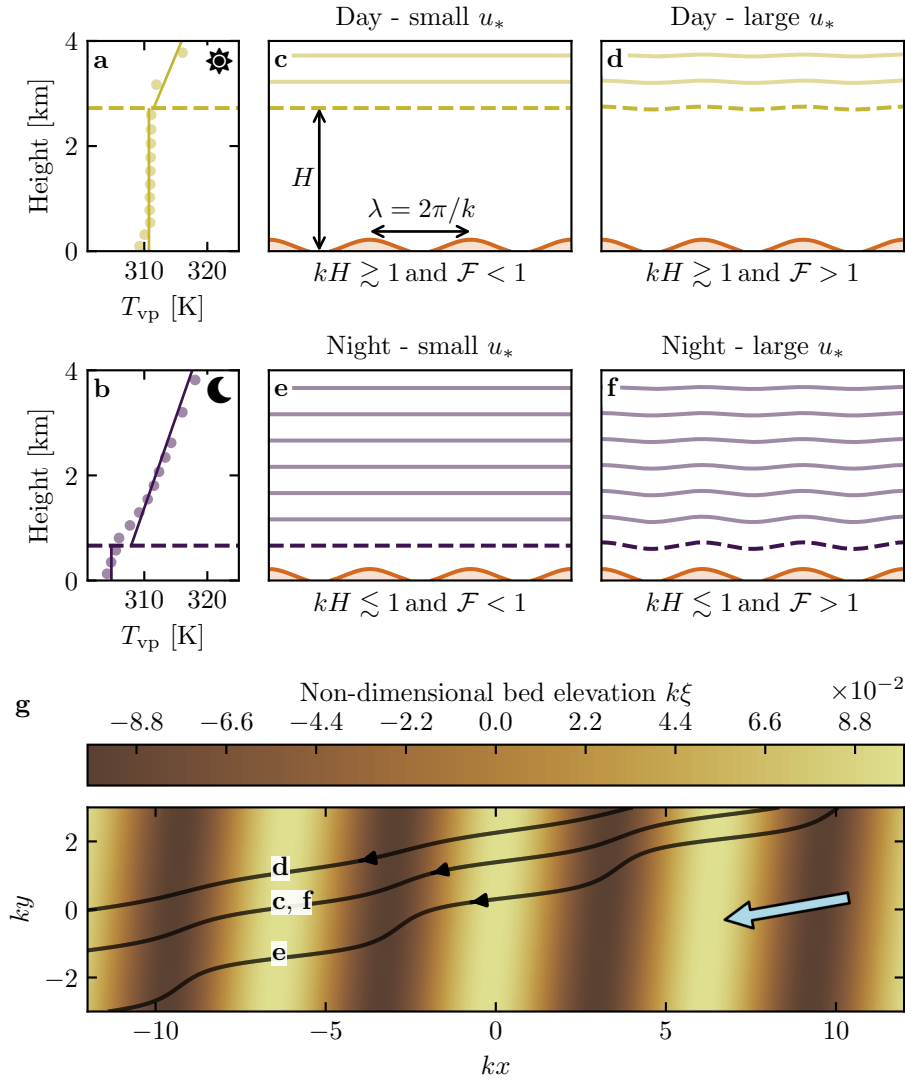


Fig. 4 **a–b:** Vertical profiles of the virtual potential temperature at 2 different time steps (day - 03/11/2015 - 1200 UTC, night - 01/13/2013 - 0900 UTC) at the North Sand Sea station. Dots: data from the ERA5 reanalysis. Dashed lines: boundary layer height given by the ERA5 reanalysis (Online Resource section 2). Plain lines: vertical (boundary layer) and linear (free atmosphere) fits to estimate the stratification properties. **c–f:** Sketches representing the interaction between the giant dunes and the atmospheric flow for different meteorological conditions. **g:** Streamlines over a sinusoidal topography $\xi(x, y)$ qualitatively representing the effect of low, medium and strong flow confinement, in relation to the above panels (see Appendix 1 for more details). The blue arrow indicates the undisturbed wind direction.

from the Bernoulli principle (Hesp et al. 2015): as the flow approaches the ridge crest, the compression of the streamlines results in larger flow velocities, and thus lower pressures (Rubin and Hunter 1987). An incident flow oblique to the ridge is then deflected towards lower pressure zones, i.e towards the crest. Turbulent dissipation tends to increase this effect downstream, resulting in wind deflection along the crest in the lee side (Gadal et al. 2019).

Flow confinement below a capping surface, which enhances streamline compression, has a strong effect on the hydrodynamic response and typically increases flow deflection. This is the case for bedforms forming in open channel flows such as rivers (Fourrière et al. 2010; Unsworth et al. 2018). This is also relevant for aeolian dunes as they evolve in the turbulent atmospheric boundary layer (ABL) capped by the stratified free atmosphere (FA) (Andreotti et al. 2009). Two main mechanisms, associated with dimensionless numbers must then be considered (Fig. 4). First, topographic obstacles typically disturb the flow over a characteristic height similar to their length. As flow confinement is characterised by a thickness H , the interaction between the dunes and the wind in the ABL is well captured by the parameter kH . The height H is directly related to the radiative fluxes at the Earth surface. It is typically on the order of a kilometre, but significantly varies with the circadian and seasonal cycles. Emerging and small dunes, with wavelengths in the range 20 to 100 m, are not affected by the confinement, corresponding to $kH \gg 1$. For giant dunes with kilometric wavelengths, however, their interaction with the FA is significant (Andreotti et al. 2009). This translates into a parameter kH in the range 0.02–5, depending on the moment of the day and the season. A second important mechanism is associated with the existence of a thin intermediate so-called capping layer between the ABL and the FA. It is characterised by a density jump $\Delta\rho$, which controls the ‘rigidity’ of this interface, i.e. how much its deformation affects streamline compression. This is usually quantified using the Froude number (Vosper 2004; Stull 2006; Sheridan and Vosper 2006; Hunt et al. 2006; Jiang 2014):

$$\mathcal{F} = \frac{U}{\sqrt{\frac{\Delta\rho}{\rho_0} g H}}, \quad (1)$$

where U is the wind velocity at the top of the ABL and ρ_0 its average density. The intensity of the stratification, i.e. the amplitude of the gradient $|\partial_z \rho|$, also impacts its ability to deform the capping layer under the presence of an underlying obstacle, and thus affects the influence of flow confinement. This can be quantified using the internal Froude number (Vosper 2004; Stull 2006; Sheridan and Vosper 2006; Hunt et al. 2006; Jiang 2014) $\mathcal{F}_I = kU/N$, where $N = \sqrt{-g\partial_z \rho/\rho_0}$ is the the Brunt-Väisälä frequency (Stull 1988). Both Froude numbers have in practice the same qualitative effect on flow confinement, and we shall restrict the main discussion to \mathcal{F} only.

With this theoretical framework in mind, and in the context of the measured wind data in the North and South Sand Sea stations, the smallest wind disturbances are expected to occur during the day, when the ABL depth is

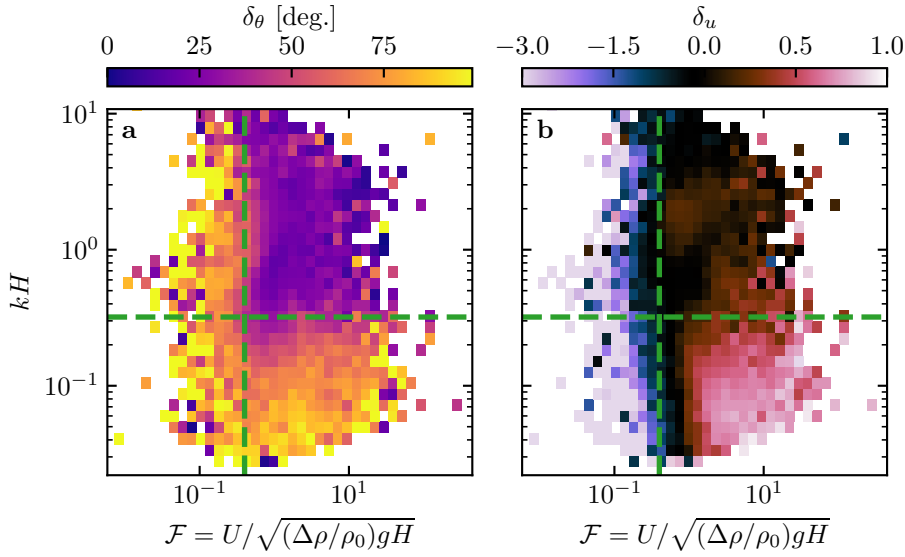


Fig. 5 Regime diagrams of the wind deviation δ_θ (a) and relative attenuation/amplification δ_u (b) in the space (\mathcal{F}, kH) , containing the data from both the North Sand Sea and South Sand Sea stations. Green dashed lines empirically delimit the different regimes. The point density in each bin of the diagrams is shown in Online Resource Fig. S14 – 95% of the data occur in the range $-1 < \delta_u < 1$. Similar regime diagrams in the spaces (\mathcal{F}_I, kH) and $(\mathcal{F}_I, \mathcal{F})$ are shown in Online Resource Fig. S15.

the largest and comparable to the dune wavelength ($kH \gtrsim 1$), which corresponds to a weak confinement situation (Fig. 4c,d). In contrast, large wind disturbances are expected to occur during the night, when the confinement is mainly induced by a shallow ABL (Fig. 4e). However, this strong confinement can be somewhat reduced in the case of strong winds, corresponding to large values of the Froude number and a less ‘rigid’ interface (Fig. 4f). This is in qualitative agreement with the transition from deflected to non-deflected winds related to low and high velocities observed in our data (Sec. 2.2).

3.2 Data distribution in the flow regimes

We can go one step further and analyse how our data quantitatively spread over the different regimes discussed above. For that purpose, one needs to compute kH and \mathcal{F} from the time series. H , U and the other atmospheric parameters can be deduced from the various vertical profiles (temperature, humidity) available in the ERA5 climate reanalysis (Online Resource section 2). We quantify the flow deflection δ_θ as the minimal angle between the wind orientations comparing the local measurements and the regional predictions. We also compute the relative velocity modulation as

$$\delta_u = \frac{u_*^{\text{ERA}} - u_*^{\text{station}}}{u_*^{\text{ERA}}}. \quad (2)$$

These two quantities are represented as maps in the plane (\mathcal{F} , kH) (Fig. 5a,b), and one can clearly identify different regions in these graphs. Small wind disturbances (small δ_θ and δ_u) are located in the top-right part of the diagrams, corresponding to a regime with low-interaction as well as low-confinement (kH and \mathcal{F} large enough, Fig. 4d). Lower values of kH (stronger interaction) or of Froude number (stronger confinement) both lead to an increase in wind disturbances, both in terms of orientation and velocity. Below a crossover value $kH \simeq 0.3$, wind disturbance is less sensitive to the \mathcal{F} -value. This is probably due to enhanced non-linear effects linked to flow modulation by the obstacle when confinement is strong. The Froude number also controls a transition from damped to amplified wind velocities in the interdune, with a crossover around $\mathcal{F} \simeq 0.4$ (Fig. 5b). Such an amplification is rather unexpected. Checking the occurrence of the corresponding data, it appears that these amplifications are associated with the southerly sea breeze, and occur dominantly during the October-March period, when the other easterly wind is not present (Online Resource Fig. S16a–b). Furthermore, they occur less frequently during the afternoon, and more frequently at the end of the day (Online Resource Fig. S16c). This effect may be linked to a change in the flow behaviour in the lee side of the obstacles but further measurements are needed in order to assess the different possibilities (Baines 1995; Vosper 2004).

4 Discussion and conclusion

The feedback of the giant dunes on the wind flow has important implications for smaller scales bedforms. As illustrated in Fig. 6, small linear dunes (~ 50 m wide) are often present in the 1–2 km interdune between giant linear dunes in the Namib Sand Sea (Livingstone et al. 2010). These smaller dunes do not exhibit the same orientation as the large ones, and are sometimes named ‘crossing dunes’. Whilst differences between large and small scale dune patterns are observed ubiquitously, they are largely attributed to the presence of two different dune growth mechanisms, leading to two different dune patterns (orientations and/or morphologies) for the same wind regime (Courrech du Pont et al. 2014; Runyon et al. 2017; Lü et al. 2017; Song et al. 2019; Gadal et al. 2020; Hu et al. 2021). Here, however, our arguments enable the development of differing orientations for the small and giant linear dunes whilst also imposing the same dune growth mechanism (elongating mode). Figure 6 shows how the orientations for the small and giant dunes can be derived from the locally measured and regionally predicted winds respectively (red arrows in Fig. 6). These predictions require a specification for the threshold of eolian sand transport. Importantly, its value expressed as a shear velocity $u_{th} \simeq 0.15 \text{ ms}^{-1}$ is reached in the deflected wind regime already. The feedback of the giant dunes on the wind described in this study thus provides a potential explanation for the existence of these small linear dunes elongating across the interdune, a dynamic which has remained unresolved to date. These crossing dunes could provide additional constraints for the inference of local winds from bedforms,

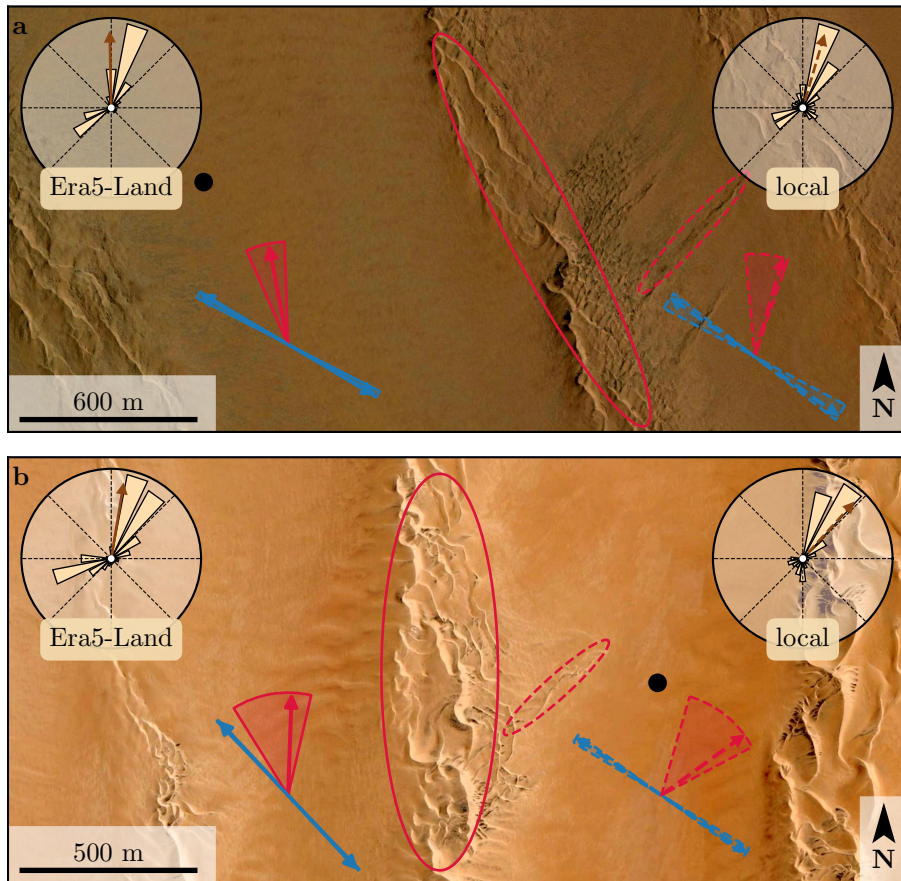


Fig. 6 Implications for smaller scale patterns in (a) the South Sand Sea and (b) North Sand Sea. The ellipses indicate the different types of elongating dunes, at large (plain line) and small (dashed line) scales. Dune orientation are predicted using the model of Courrech du Pont et al. (2014) from the sand flux angular distributions, shown here (roses and resultant transport direction) for typical values (grain size $180 \mu\text{m}$, flux-up ratio of 1.6). Code for corresponding arrows: use of ERA5-Land data (plain line), use of local measurements (dashed line), prediction for the bed instability growth mechanism (blue), prediction for the elongation growth mechanism (red). Wedges show the uncertainty on the orientation calculation when parameters are varied. The black dots indicate the location of the meteorological stations with respect to the dunes. See Appendix 2 for additional details.

322 similarly to that currently performed on Mars using ripple orientations (Liu
323 and Zimbelman 2015; Hood et al. 2021). Further work is needed to investigate
324 these processes in more detail, including measurements of sediment transport
325 and flow on the top of dunes.

326 This study presents the evidence that wind flow patterns around giant
327 dunes are influenced by the atmospheric boundary layer, particularly during
328 nocturnal conditions. It leaves open the debate as to whether the size of giant
329 dunes is limited by the depth of this layer (Andreotti et al. 2009), in contrast to

330 an unconstrained dune growth, ever-slower with size (Gunn et al. 2021). More
331 field evidence is needed from additional dune fields, but this mechanism would
332 then allow for the inference of the ABL depth from giant bedform wavelengths
333 where measurements are not feasible or available, such as Titan (Lorenz et al.
334 2010).

335 To conclude on conditions under which the ERA5-Land reanalysis data can
336 reliably be used to study dune morphodynamics, we summarise the compari-
337 son of local (direct measurements) and regional (climate reanalysis) wind data.
338 In flat areas, the agreement between the two confirms the ability of the ERA5-
339 Land climate reanalysis to predict the wind regime down to scales ~ 10 km,
340 i.e. the model grid. When smaller scale topographies are present (giant dunes
341 in our case), locally measured winds can significantly differ from the regionally
342 predicted ones. This is the case when the disturbances induced by the dunes
343 interact with the lower part of the ABL vertical structure, which presents cir-
344 cadian variations. During the day, when the capping layer is typically high,
345 this interaction is small, and the ERA5-Land predictions are also quantita-
346 tively consistent with the local data. During the night, however, the presence
347 of a shallow atmospheric boundary layer induces a strong confinement of the
348 flow, and is associated with large wind deflection by the dunes. Importantly,
349 we find that this effect can be counterbalanced for large wind velocities, which
350 are capable of deforming the capping layer, thus decreasing the influence of
351 the confinement.

352 The theoretical computation of the wind disturbances induced by sinu-
353 soidal ridges under flow confinement has been performed in the linear limit
354 (Andreotti et al. 2009, 2012), i.e. when the aspect ratio of these ridges is small
355 ($k\xi_0 \ll 1$). These models are able to qualitatively reproduce the observed wind
356 deflection (Appendix 1, Online Resource Figs. S15 and S17), and thus provide
357 the physical support for the interpretation we propose here based on hydro-
358 dynamic regimes. However, these models cannot quantitatively predict the
359 magnitude of these observations, probably due to the presence of expected
360 non-linearities in high confinement situations linked to strong flow modula-
361 tions. Besides, these linear calculations only predict wind attenuation in the
362 interdune, in contrast with the observed enhanced velocities associated with
363 particular evening winds from the South during the period October-March
364 (Online Resource Fig. S16). Some other models predict different spatial flow
365 structures in response to a modulated topography, such as lee waves and rotors
366 (Baines 1995; Vosper 2004). However, our measurements are located at a single
367 point in the interdune, so we are unable to explore these types of responses.
368 Data at different places along and across the ridges are needed to investigate
369 and possibly map such flow structures, and for further comparisons with the
370 models.

371 **Acknowledgements** We would like to acknowledge the contributors of the following open-
372 source python libraries, Matplotlib (Hunter 2007), Numpy (Harris et al. 2020) and Scipy
373 (Virtanen et al. 2020), which provide an incredibly efficient ecosystem allowing scientific
374 research in Python.

375 All data used in this study can be found in Gadal et al. (2022). Note that it contains
 376 modified Copernicus Climate Change Service Information (2021). Neither the European
 377 Commission nor ECMWF is responsible for any use that may be made of the Copernicus
 378 Information or Data it contains. Fully documented codes used to analyse this study are
 379 available at <https://github.com/Cgadal/GiantDunes> (will be made public upon acceptance
 380 of this manuscript for publication).

381 Multiple grants have supported the collection of wind data through visits to the four
 382 sites between 2013 and 2020 (John Fell Oxford University Press (OUP) Research Fund
 383 (121/474); National Geographic (CP-029R-17); Natural Environment Research Council UK
 384 (NE/R010196/1 and NE/H021841/1 NSFGEO-NERC); Southampton Marine and Maritime
 385 Institute SMMI EPSRC-GCRF UK), along with research permits (1978/2014, 2140/2016,
 386 2304/2017, 2308/2017, RPIV00022018, RPIV0052018, RPIV00230218). The authors are
 387 very grateful for support from Etosha National Park (especially Shyane Köting, Boas Er-
 388 kieke, Pierre du Preez, Claudine Cloete, Immanuel Kapofi, Wilferd Versfeld, and Werner
 389 Kilian), Gobabeb Namib Research Institute (Gillian Maggs-Kölling and Eugene Marais),
 390 The Skeleton Coast National Park (Joshua Kazuerua). Various researchers and desert en-
 391 thusiasts have assisted with instruments and the logistics of expeditions, especially Mary
 392 Seely for expert guidance at the North Sand Sea site.

393 Finally, we acknowledge financial support from the Laboratoire d'Excellence UnivEarthS
 394 Grant ANR-10-LABX-0023, the Initiative d'Excellence Université de Paris Grant ANR-18-
 395 IDEX-0001, the French National Research Agency Grants ANR-17-CE01-0014/SONO and
 396 the National Science Center of Poland Grant 2016/23/B/ST10/01700.

397 Appendix 1: Linear theory of wind response to topographic pertur- 398 bation

399 Following the work of Fourrière et al. (2010), Andreotti et al. (2012) and
 400 Andreotti et al. (2009), we briefly describe in this appendix the framework
 401 for the linear response of a turbulent flow to a topographic perturbation of
 402 small aspect ratio. As a general bed elevation can be decomposed into Fourier
 403 modes, we focus here on a sinusoidal topography:

$$\xi = \xi_0 \cos [k (\cos(\alpha)y - \sin(\alpha)x)], \quad (3)$$

404 which is also a good approximation for the giant dunes observed in the North
 405 Sand Sea and South Sand Sea Station (Fig. 1 and Online Resource Fig. S5).
 406 Here, x and y are the streamwise and spanwise coordinates, $k = 2\pi/\lambda$ the
 407 wavenumber of the sinusoidal perturbation, α its crest orientation with respect
 408 to the x -direction (anticlockwise) and ξ_0 its amplitude. The two components
 409 of the basal shear stress $\tau = \rho_0 u_* \mathbf{u}_*$, constant in the flat bottom reference
 410 case, can then be generically written as:

$$\tau_x = \tau_0 \left(1 + k \xi_0 \sqrt{\mathcal{A}_x^2 + \mathcal{B}_x^2} \cos [k (\cos(\alpha)y - \sin(\alpha)x) + \phi_x] \right), \quad (4)$$

$$\tau_y = \tau_0 k \xi_0 \sqrt{\mathcal{A}_y^2 + \mathcal{B}_y^2} \cos [k (\cos(\alpha)y - \sin(\alpha)x) + \phi_y], \quad (5)$$

411 where τ_0 is the reference basal shear stress on a flat bed. We have defined
 412 the phase $\phi_{x,y} = \tan^{-1}(\mathcal{B}_{x,y}/\mathcal{A}_{x,y})$ from the in-phase and in-quadrature hy-
 413 drodynamical coefficients $\mathcal{A}_{x,y}$ and $\mathcal{B}_{x,y}$. They are functions of k and of the
 414 flow conditions, i.e the bottom roughness, the vertical flow structure and the

⁴¹⁵ incident flow direction, and the theoretical framework developed in the above
⁴¹⁶ cited papers proposes methods to compute them in the linear regime.

⁴¹⁷ Following Andreotti et al. (2012), the effect of the incident wind direction
⁴¹⁸ can be approximated by the following expressions:

$$\mathcal{A}_x = \mathcal{A}_0 \sin^2 \alpha, \quad (6)$$

$$\mathcal{B}_x = \mathcal{B}_0 \sin^2 \alpha, \quad (7)$$

$$\mathcal{A}_y = -\frac{1}{2} \mathcal{A}_0 \cos \alpha \sin \alpha, \quad (8)$$

$$\mathcal{B}_y = -\frac{1}{2} \mathcal{B}_0 \cos \alpha \sin \alpha, \quad (9)$$

⁴¹⁹ where \mathcal{A}_0 and \mathcal{B}_0 are now two coefficients independent of the dune orientation
⁴²⁰ α , corresponding to the transverse case ($\alpha = 90^\circ$). For a fully turbulent
⁴²¹ boundary layer capped by a stratified atmosphere, these coefficients depend
⁴²² on kH , kz_0 , \mathcal{F} and \mathcal{F}_1 (Andreotti et al. 2009). In this study, we assume a con-
⁴²³ stant hydrodynamic roughness $z_0 \simeq 1$ mm (Online Resource section 1). For
⁴²⁴ the considered giant dunes, this leads to $kz_0 \simeq 2 \cdot 10^{-6}$, as their wavelength
⁴²⁵ is $\lambda \simeq 2.4$ km (or $k \simeq 2 \cdot 10^{-3}$ m⁻¹). Values of z_0 extracted from field data
⁴²⁶ indeed typically fall between 0.1 mm and 10 mm (Sherman and Farrell 2008;
⁴²⁷ Field and Pelletier 2018). Importantly, \mathcal{A}_0 and \mathcal{B}_0 do not vary much in the
⁴²⁸ corresponding range of kz_0 (Fourrière et al. 2010), and the results presented
⁴²⁹ here are robust with respect to this choice.

⁴³⁰ With capping layer height and Froude numbers computed from the ERA5-
⁴³¹ Land time series, the corresponding \mathcal{A}_0 and \mathcal{B}_0 can be deduced, as displayed
⁴³² in Online Resource Fig. S17. Interestingly, it shows similar regimes as in the
⁴³³ diagrams of Fig. 5 and Online Resource Fig. S15a,b, supporting the underly-
⁴³⁴ ing physics. However, the agreement is qualitative only. Further, the linearity
⁴³⁵ assumption of the theoretical framework requires $(|\tau| - \tau_0)/\tau_0 \ll 1$, which
⁴³⁶ translates into $k\xi \sqrt{\mathcal{A}_0^2 + \mathcal{B}_0^2} \ll 1$. In our case, the giant dune morphology
⁴³⁷ gives $k\xi_0 \simeq 0.1$, which means that one quits the regime of validity of the
⁴³⁸ linear theory when the coefficient modulus $\sqrt{\mathcal{A}_0^2 + \mathcal{B}_0^2}$ becomes larger than a
⁴³⁹ few units. In accordance with the theoretical expectations, these coefficients
⁴⁴⁰ present values on the order of unity ($\mathcal{A}_0 \simeq 3$ and $\mathcal{B}_0 \simeq 1$) in unconfined sit-
⁴⁴¹ uations (Claudin et al. 2013; Lü et al. 2021). In contrast and as illustrated
⁴⁴² in Online Resource Fig. S17a,b, larger values are predicted in case of strong
⁴⁴³ confinement, which does not allow us to proceed to further quantitative com-
⁴⁴⁴ parison with the data.

⁴⁴⁵ Finally, the linear model is also able to reproduce the enhancement of the
⁴⁴⁶ flow deflection over the sinusoidal ridges when $\sqrt{\mathcal{A}_0^2 + \mathcal{B}_0^2}$ is increased (Online
⁴⁴⁷ Resource Fig. S17). Here, using $k\xi_0 \simeq 0.1$ to be representative of the amplitude
⁴⁴⁸ of the giant dunes at the North Sand Sea station, the coefficient modulus is
⁴⁴⁹ bounded to 10.

450 Appendix 2: Sediment transport and dune morphodynamics

451 We summarise in this appendix the sediment transport and dune morphodynamics
 452 theoretical framework leading to the prediction of sand fluxes and dune
 453 orientations from wind data.

454 *Sediment transport* — The prediction of sand fluxes from wind data has been
 455 a long standing issue in aeolian geomorphological studies (Fryberger and Dean
 456 1979; Pearce and Walker 2005; Sherman and Li 2012; Shen et al. 2019). Based
 457 on laboratory studies in wind tunnels (Rasmussen et al. 1996; Iversen and
 458 Rasmussen 1999; Creyssels et al. 2009; Ho et al. 2011), as well as physical
 459 considerations (Ungar and Haff 1987; Andreotti 2004; Durán et al. 2011; Pähzt
 460 and Durán 2020), it has been shown that the steady saturated saltation flux
 461 over a flat sand bed depends linearly on the shear stress:

$$\frac{q_{\text{sat}}}{Q} = \Omega \sqrt{\Theta_{\text{th}}} (\Theta - \Theta_{\text{th}}), \quad (10)$$

462 where Ω is a proportionality constant, $Q = d\sqrt{(\rho_s - \rho_0)gd/\rho_0}$ is a character-
 463 istic flux, $\Theta = \rho_0 u_*^2 / (\rho_s - \rho_0)gd$ the Shields number, and Θ_{th} its threshold
 464 value below which saltation vanishes. $\rho_s = 2.6 \text{ g cm}^{-3}$ and $d = 180 \mu\text{m}$ are
 465 the grain density and diameter, and g is the gravitational acceleration. The
 466 shear velocity, and consequently the Shields number as well as the sediment
 467 flux, are time dependent.

468 Recently, Pähzt and Durán (2020) suggested an additional quadratic term
 469 in Shields to account for grain-grain interactions within the transport layer at
 470 strong wind velocities:

$$\frac{q_{\text{sat}, t}}{Q} = \frac{2\sqrt{\Theta_{\text{th}}}}{\kappa\mu} (\Theta - \Theta_{\text{th}}) \left(1 + \frac{C_M}{\mu} [\Theta - \Theta_{\text{th}}] \right), \quad (11)$$

471 where $\kappa = 0.4$ is the von Kármán constant, $C_M \simeq 1.7$ a constant and $\mu \simeq 0.6$ is
 472 a friction coefficient, taken to be the avalanche slope of the granular material.
 473 The fit of this law to the experimental data of Creyssels et al. (2009) and Ho
 474 et al. (2011) gives $\Theta_{\text{th}} = 0.0035$. The fit of Eq. 10 on these same data similarly
 475 gives $\Omega \simeq 8$ and $\Theta_{\text{th}} = 0.005$. The sand flux angular distributions and the
 476 dune orientations in Fig. 6 are calculated using this law (11). We have checked
 477 that using the ordinary linear relationship (10) instead does not change the
 478 predicted dune orientations by more than a few degrees.

479 *Dune orientations* — Dune orientations are predicted with the dimensional
 480 model of Courrech du Pont et al. (2014), from the sand flux time series com-
 481 puted with the above transport law. Two orientations are possible depending
 482 on the mechanism dominating the dune growth: elongation or bed instabil-
 483 ity. The orientation α corresponding the bed instability is then the one that
 484 maximises the following growth rate (Rubin and Hunter 1987):

$$\sigma \propto \frac{1}{H_d W_d T} \int_0^T q_{\text{crest}} |\sin(\theta - \alpha)| dt, \quad (12)$$

485 where θ is the wind orientation measured with respect to the same reference
 486 as α , and H_d and W_d are dimensional constants respectively representing the
 487 dune height and width. The integral runs over a time T , which must be repre-
 488 sentative of the characteristic period of the wind regime. The flux at the crest
 489 is expressed as:

$$q_{\text{crest}} = q_{\text{sat}} [1 + \gamma |\sin(\theta - \alpha)|], \quad (13)$$

490 where the flux-up ratio γ has been calibrated to 1.6 using field studies, under-
 491 water laboratory experiments and numerical simulations. Predictions of the
 492 linear analysis of Gadal et al. (2019) and Delorme et al. (2020) give similar
 493 results.

494 Similarly, the dune orientation corresponding to the elongation mechanism
 495 is the one that verifies:

$$\tan(\alpha) = \frac{\langle q_{\text{crest}}(\alpha) \mathbf{e}_\theta \rangle \cdot \mathbf{e}_{WE}}{\langle q_{\text{crest}}(\alpha) \mathbf{e}_\theta \rangle \cdot \mathbf{e}_{SN}}, \quad (14)$$

496 where $\langle \cdot \rangle$ denotes a vectorial time average. The unitary vectors \mathbf{e}_{WE} , \mathbf{e}_{SN} and
 497 \mathbf{e}_θ are in the West-East, South-North and wind directions, respectively.

498 The resulting computed dune orientations, blue and red arrows in Fig. 6,
 499 then depend on a certain number of parameters (grain properties, flux-up ratio,
 500 etc.), for which we take typical values for aeolian sandy deserts. Due to the lack
 501 of measurements in the studied places, some uncertainties can be expected. We
 502 therefore run a sensitivity test by calculating the dune orientations for grain
 503 diameters ranging from 100 μm to 400 μm and for a speed-up ratio between
 504 0.1 and 10 (wedges in Fig. 6).

References

- 505 Andreotti B (2004) A two-species model of aeolian sand transport. *J Fluid
Mech* 510:47–70
- 508 Andreotti B, Claudin P, Douady S (2002) Selection of dune shapes and veloc-
509 ities part 1: Dynamics of sand, wind and barchans. *The European Physical
510 Journal B-Condensed Matter and Complex Systems* 28(3):321–339
- 511 Andreotti B, Fourrière A, Ould-Kaddour F, Murray B, Claudin P (2009) Gi-
512 ant aeolian dune size determined by the average depth of the atmospheric
513 boundary layer. *Nature* 457:1120–1123
- 514 Andreotti B, Claudin P, Devauchelle O, Durán O, Fourrière A (2012) Bedforms
515 in a turbulent stream: ripples, chevrons and antidunes. *J Fluid Mech* 690:94–
516 128
- 517 Ashkenazy Y, Yizhaq H, Tsoar H (2012) Sand dune mobility under climate
518 change in the kalahari and australian deserts. *Climatic Change* 112:901–923
- 519 Baddock M, Livingstone I, Wiggs G (2007) The geomorphological significance
520 of airflow patterns in transverse dune interdunes. *Geomorphology* 87:322–
521 336
- 522 Baines PG (1995) Topographic effects in stratified flows. Cambridge university
523 press
- 524 Bauer BO, Sherman DJ, Wolcott JF (1992) Sources of uncertainty in shear
525 stress and roughness length estimates derived from velocity profiles. *The
526 Professional Geographer* 44:453–464
- 527 Belcher S, JCR H (1998) Turbulent flow over hills and waves. *Annu Rev Fluid
528 Mech* 30:507–538
- 529 Blumberg DG, Greeley R (1996) A comparison of general circulation model
530 predictions to sand drift and dune orientations. *J Clim* 9:3248–3259
- 531 Bristow NR, Best J, Wiggs GFS, Nield JM, Baddock MC, Delorme P, Chris-
532 tensen KT (2022) Topographic perturbation of turbulent boundary layers
533 by low-angle, early-stage aeolian dunes. *Earth Surf Process Landf* n/a(n/a),
534 DOI <https://doi.org/10.1002/esp.5326>
- 535 Brown S, Nickling WG, Gillies JA (2008) A wind tunnel examination of shear
536 stress partitioning for an assortment of surface roughness distributions. *J
537 Geophys Res* 113:F02S06
- 538 Charru F, Andreotti B, Claudin P (2013) Sand ripples and dunes. *Annu Rev
539 Fluid Mech* 45:469–493
- 540 Claudin P, Wiggs G, Andreotti B (2013) Field evidence for the upwind velocity
541 shift at the crest of low dunes. *Boundary-Layer Meteorol* 148:195–206
- 542 Claudin P, Durán O, Andreotti B (2017) Dissolution instability and roughen-
543 ing transition. *J Fluid Mech* 832:R2
- 544 Claudin P, Louge M, Andreotti B (2021) Basal pressure variations induced by
545 a turbulent flow over a wavy surface. *Frontiers in Physics* 9:682564
- 546 Courrech du Pont S (2015) Dune morphodynamics. *C R Phys* 16:118–138
- 547 Courrech du Pont S, Narteau C, Gao X (2014) Two modes for dune orientation.
548 *Geology* 42:743–746

- 549 Creyssels M, Dupont P, El Moctar AO, Valance A, Cantat I, Jenkins JT, Pasini
550 JM, Rasmussen KR (2009) Saltating particles in a turbulent boundary layer:
551 experiment and theory. *J Fluid Mech* 625:47–74
- 552 de Winter W, Donker J, Sterk G, Van Beem J, Ruessink G (2020) Regional
553 versus local wind speed and direction at a narrow beach with a high and
554 steep foredune. *Plos one* 15(1):e0226983
- 555 Dee DP, Uppala SM, Simmons AJ, Berrisford P, Poli P, Kobayashi S, Andrae
556 U, Balmaseda M, Balsamo G, Bauer dP, et al. (2011) The era-interim re-
557 analysis: Configuration and performance of the data assimilation system. *Q*
558 *J R Meteorol Soc* 137:553–597
- 559 Delorme P, Wiggs G, Baddock M, Claudin P, Nield J, Valdez A (2020) Dune
560 initiation in a bimodal wind regime. *J Geophys Res* 125:e2020JF005757
- 561 Durán O, Claudin P, Andreotti B (2011) On aeolian transport: Grain-scale
562 interactions, dynamical mechanisms and scaling laws. *Aeolian Res* 3:243–
563 270
- 564 Durran DR (1990) Mountain waves and downslope winds. In: *Atmospheric*
565 *processes over complex terrain*, Springer, pp 59–81
- 566 Farr TG, Rosen PA, Caro E, Crippen R, Duren R, Hensley S, Kobrick M,
567 Paller M, Rodriguez E, Roth L, et al. (2007) The shuttle radar topography
568 mission. *Rev Geophys* 45
- 569 Fernando H, Mann J, Palma J, Lundquist JK, Barthelmie RJ, Belo-Pereira M,
570 Brown W, Chow F, Gerz T, Hocut C, et al. (2019) The perdigão: Peering
571 into microscale details of mountain winds. *Bull Am Meteorol Soc* 100:799–
572 819
- 573 Field JP, Pelletier JD (2018) Controls on the aerodynamic roughness length
574 and the grain-size dependence of aeolian sediment transport. *Earth Surf*
575 *Process Landf* 43:2616–2626
- 576 Finnigan J, Raupach M, Bradley E, Aldis G (1990) A wind tunnel study
577 of turbulent flow over a two-dimensional ridge. *Boundary-Layer Meteorol*
578 50:277–317
- 579 Finnigan J, Ayotte K, Harman I, Katul G, Oldroyd H, Patton E, Poggi D,
580 Ross A, Taylor P (2020) Boundary-layer flow over complex topography.
581 *Boundary-Layer Meteorol* 177:247–313
- 582 Flack K, Schultz M (2010) Review of hydraulic roughness scales in the fully
583 rough regime. *Journal of Fluids Engineering* 132:041203
- 584 Fourrière A, Claudin P, Andreotti B (2010) Bedforms in a turbulent stream:
585 formation of ripples by primary linear instability and of dunes by nonlinear
586 pattern coarsening. *J Fluid Mech* 649:287–328
- 587 Frederick KA, Hanratty TJ (1988) Velocity measurements for a turbulent non-
588 separated flow over solid waves. *Exp Fluids* 6:477–486
- 589 Fryberger SG, Dean G (1979) Dune forms and wind regime. A study of global
590 sand seas 1052:137–169
- 591 Gadal C, Narteau C, Courrech Du Pont S, Rozier O, Claudin P (2019) Incip-
592 ient bedforms in a bidirectional wind regime. *J Fluid Mech* 862:490–516
- 593 Gadal C, Narteau C, Courrech du Pont S, Rozier O, Claudin P (2020) Peri-
594 odicity in fields of elongating dunes. *Geology* 48:343–347

- 595 Gadal C, Delorme P, Narteau C, Wiggs G, Baddock M, Nield JM, Claudin
596 P (2022) Data used in 'Local wind regime induced by giant linear dunes:
597 comparison of ERA5-Land re-analysis with surface measurements'. DOI
598 10.5281/zenodo.6343138
- 599 Garvey B, Castro IP, Wiggs G, Bullard J (2005) Measurements of flows over
600 isolated valleys. *Boundary-Layer Meteorol* 117(3):417–446
- 601 Gong W, Ibbetson A (1989) A wind tunnel study of turbulent flow over model
602 hills. *Boundary-Layer Meteorol* 49:113–148
- 603 Gong W, Taylor P, Dörnbrack A (1996) Turbulent boundary-layer flow over
604 fixed aerodynamically rough two-dimensional sinusoidal waves. *J Fluid Mech*
605 312:1–37
- 606 Gunn A, Casasanta G, Di Liberto L, Falcini F, Lancaster N,
607 Jerolmack DJ (2021) What sets aeolian dune height? DOI
608 <https://doi.org/10.31223/X5QG8S>
- 609 Harris CR, Millman KJ, van der Walt SJ, Gommers R, Virtanen P, Cournapeau D,
610 Wieser E, Taylor J, Berg S, Smith NJ, et al. (2020) Array programming with
611 numpy. *Nature* 585:357–362
- 612 Hersbach H, Bell B, Berrisford P, Hirahara S, Horányi A, Muñoz-Sabater J,
613 Nicolas J, Peubey C, Radu R, Schepers D, et al. (2020) The era5 global
614 reanalysis. *Q J R Meteorol Soc* 146:1999–2049
- 615 Hesp PA, Hastings K (1998) Width, height and slope relationships and aero-
616 dynamic maintenance of barchans. *Geomorphology* 22(2):193–204
- 617 Hesp PA, Smyth TAG, Nielsen P, Walker IJ, Bauer BO, Davidson-Arnott R
618 (2015) Flow deflection over a foredune. *Geomorphology* 230:64–74
- 619 Ho TD, Valance A, Dupont P, Ould El Moctar A, Tuan Duc H, Valance A,
620 Dupont P, Ould El Moctar A (2011) Scaling laws in aeolian sand transport.
621 *Phys Rev Lett* 106:4–7
- 622 Hood DR, Ewing RC, Roback KP, Runyon K, Avouac JP, McEnroe M (2021)
623 Inferring airflow across martian dunes from ripple patterns and dynamics.
624 *Frontiers in Earth Science* 9:702828
- 625 Howard AD (1977) Effect of slope on the threshold of motion and its applica-
626 tion to orientation of wind ripples. *Geological Society of America Bulletin*
627 88:853–856
- 628 Hu Z, Gao X, Lei J, Zhou N (2021) Geomorphology of aeolian dunes in the
629 western sahara desert. *Geomorphology* 392:107916
- 630 Hunt J, Leibovich S, Richards K (1988) Turbulent shear flows over low hills.
631 *Q J R Meteorol Soc* 114:1435–1470
- 632 Hunt JCR, Vilenski GG, Johnson ER (2006) Stratified separated flow around
633 a mountain with an inversion layer below the mountain top. *J Fluid Mech*
634 556:105–119
- 635 Hunter JD (2007) Matplotlib: A 2d graphics environment. *Computing in sci-
636 ence & engineering* 9:90–95
- 637 Iversen JD, Rasmussen KR (1999) The effect of wind speed and bed slope on
638 sand transport. *Sedimentology* 46:723–731
- 639 Jackson PS, Hunt JCR (1975) Turbulent wind flow over a low hill. *Q J R
640 Meteorol Soc* 101:929–955

- 641 Jiang Q (2014) Applicability of reduced-gravity shallow-water theory to atmo-
642 spheric flow over topography. *J Atmos Sci* 71:1460–1479
- 643 Jolivet M, Braucher R, Dovchintseren D, Hocquet S, Schmitt J, ASTER Team
644 (2021) Erosion around a large-scale topographic high in a semi-arid sedimentary basin: Interactions between fluvial erosion, aeolian erosion and aeolian
645 transport. *Geomorphology* 386:107747
- 646 Kim HG, Patel VC, Lee CM (2000) Numerical simulation of wind flow over
647 hilly terrain. *J Wind Eng Ind Aerodyn* 87:45–60
- 648 Lancaster J, Lancaster N, Seely M (1984) Climate of the central namib desert.
649 Madoqua 1984:5–61
- 650 Lancaster N (1985) Winds and sand movements in the namib sand sea. *Earth
651 Surf Process Landf* 10:607–619
- 652 Lancaster N, Nickling W, Neuman CM, Wyatt V (1996) Sediment flux and
653 airflow on the stoss slope of a barchan dune. *Geomorphology* 17(1-3):55–62
- 654 Lewis HW, Mobbs SD, Lehning M (2008) Observations of cross-ridge flows
655 across steep terrain. *Q J R Meteorol Soc* 134:801–816
- 656 Liu ZYC, Zimbelman JR (2015) Recent near-surface wind directions inferred
657 from mapping sand ripples on martian dunes. *Icarus* 261:169–181
- 658 Livingstone I, Warren A (2019) Aeolian geomorphology: a new introduction.
659 Wiley
- 660 Livingstone I, Bristow C, Bryant RG, Bullard J, White K, Wiggs GFS, Baas
661 ACW, Bateman MD, Thomas DSG (2010) The namib sand sea digital
662 database of aeolian dunes and key forcing variables. *Aeolian Res* 2:93–104
- 663 Lorenz R, Claudin P, Andreotti B, Radebaugh J, Tokano T (2010) A 3 km
664 atmospheric boundary layer on titan indicated by dune spacing and huygens
665 data. *Icarus* 205:719–721
- 666 Lü P, Narteau C, Dong Z, Rozier O, Du Pont SC (2017) Unravelling raked
667 linear dunes to explain the coexistence of bedforms in complex dunefields.
668 Nature communications 8:1–9
- 669 Lü P, Narteau C, Dong Z, Claudin P, Rodriguez S, An Z, Fernandez-Cascales
670 L, Gadal C, Courrech du Pont S (2021) Direct validation of dune instability
671 theory. *Proceedings of the National Academy of Sciences* 118
- 672 Mason P, Sykes R (1979) Flow over an isolated hill of moderate slope. *Q J R
673 Meteorol Soc* 105:383–395
- 674 McKenna Neuman C, Lancaster N, Nickling WG (1997) Relations between
675 dune morphology, air flow, and sediment flux on reversing dunes, Sil-
676 ver Peak, Nevada. *Sedimentology* 44(6):1103–1111, DOI 10.1046/j.1365-
677 3091.1997.d01-61.x
- 678 Muñoz-Sabater J, Dutra E, Agustí-Panareda A, Albergel C, Arduini G, Bal-
679 samsó G, Boussetta S, Choulga M, Harrigan S, Hersbach H, et al. (2021)
680 Era5-land: A state-of-the-art global reanalysis dataset for land applications.
681 *Earth Syst Sci Data* 13:4349–4383
- 682 Nield JM, King J, Wiggs GFS, Leyland J, Bryant RG, Chiverrell RC, Darby
683 SE, Eckhardt FD, Thomas DSG, Vircavs LH, Washington R (2014) Esti-
684 mating aerodynamic roughness over complex surface terrain. *J Geophys Res*
685 118:12948–12961

- 687 Nield JM, Wiggs GF, Baddock MC, Hipondoka MH (2017) Coupling leeside
688 grainfall to avalanche characteristics in aeolian dune dynamics. *Geology*
689 45(3):271–274
- 690 Pähzt T, Durán O (2020) Unification of aeolian and fluvial sediment transport
691 rate from granular physics. *Phys Rev Lett* 124:168001
- 692 Pearce KI, Walker IJ (2005) Frequency and magnitude biases in the 'Fryberger'
693 model, with implications for characterizing geomorphically effective winds.
694 *Geomorphology* 68:39–55
- 695 Pelletier JD, Field JP (2016) Predicting the roughness length of turbulent flows
696 over landscapes with multi-scale microtopography. *Earth Surface Dynamics*
697 4:391–405
- 698 Poggi D, Katul G, Albertson J, Ridolfi L (2007) An experimental investigation
699 of turbulent flows over a hilly surface. *Phys Fluids* 19:036601
- 700 Rasmussen KR, Iversen JD, Rautaheimo P (1996) Saltation and wind flow
701 interaction in a variable slope wind tunnel. *Geomorphology* 17:19–28
- 702 Raupach M (1992) Drag and drag partition on rough surfaces. *Boundary-Layer
703 Meteorol* 60:375–395
- 704 Rubin DM, Hunter RE (1987) Bedform alignment in directionally varying
705 flows. *Science* 237:276–278
- 706 Runyon K, Bridges N, Ayoub F, Newman C, Quade J (2017) An integrated
707 model for dune morphology and sand fluxes on mars. *Earth and Planetary
708 Science Letters* 457:204–212
- 709 Sauermann G, Andrade Jr J, Maia L, Costa U, Araújo A, Herrmann H (2003)
710 Wind velocity and sand transport on a barchan dune. *Geomorphology* 54(3–
711 4):245–255
- 712 Seidel DJ, Zhang Y, Beljaars A, Golaz JC, Jacobson AR, Medeiros B (2012)
713 Climatology of the planetary boundary layer over the continental united
714 states and europe. *J Geophys Res* 117:D17106
- 715 Shao Y (2008) Physics and modelling of wind erosion, vol 37. Springer Science
716 & Business Media
- 717 Shen Y, Zhang C, Huang X, Wang X, Cen S (2019) The effect of wind speed
718 averaging time on sand transport estimates. *Catena* 175:286–293
- 719 Sheridan PF, Vosper SB (2006) A flow regime diagram for forecasting lee
720 waves, rotors and downslope winds. *Meteorol Appl* 13:179–195
- 721 Sherman D, Farrell E (2008) Aerodynamic roughness lengths over movable
722 beds: Comparison of wind tunnel and field data. *J Geophys Res* 113:1–10
- 723 Sherman DJ, Li B (2012) Predicting aeolian sand transport rates: A reevalu-
724 ation of models. *Aeolian Res* 3:371–378
- 725 Smith AB, Jackson DWT, Cooper JAG (2017) Three-dimensional airflow and
726 sediment transport patterns over barchan dunes. *Geomorphology* 278:28–42
- 727 Song Q, Gao X, Lei J, Li S (2019) Spatial distribution of sand dunes and their
728 relationship with fluvial systems on the southern margin of the taklimakan
729 desert, china. *Geomatics, Natural Hazards and Risk* 10:2408–2428
- 730 Spalding DB (1961) A single formula for the law of the wall. *Journal of Applied
731 Mechanics* 28:455–458

- 732 Stull R (2006) 9 - the atmospheric boundary layer. In: Wallace JM, Hobbs PV
733 (eds) *Atmospheric Science* (Second Edition), second edition edn, Academic
734 Press, San Diego, pp 375–417
- 735 Stull RB (1988) An introduction to boundary layer meteorology, vol 13.
736 Springer Science & Business Media
- 737 Sullivan PP, McWilliams JC (2010) Dynamics of winds and currents coupled
738 to surface waves. *Annu Rev Fluid Mech* 42:19–42
- 739 Sykes RI (1980) An asymptotic theory of incompressible turbulent boundary-
740 layer flow over a small hump. *J Fluid Mech* 101:647–670
- 741 Taylor P, Teunissen H (1987) The Askervein hill project: overview and back-
742 ground data. *Boundary-Layer Meteorol* 39:15–39
- 743 Taylor P, Mason P, Bradley E (1987) Boundary-layer flow over low hills.
744 *Boundary-Layer Meteorol* 39:107–132
- 745 Ungar JE, Haff PK (1987) Steady state saltation in air. *Sedimentology* 34:289–
746 299
- 747 Unsworth C, Parsons D, Hardy R, Reesink A, Best J, Ashworth P, Keevil G
748 (2018) The impact of nonequilibrium flow on the structure of turbulence
749 over river dunes. *Water Resour Res* 54:6566–6584
- 750 Uppala SM, Källberg P, Simmons AJ, Andrae U, Bechtold VDC, Fiorino M,
751 Gibson J, Haseler J, Hernandez A, Kelly G, et al. (2005) The era-40 re-
752 analysis. *Q J R Meteorol Soc* 131:2961–3012
- 753 Valance A, Rasmussen K, Ould El Moctar A, Dupont P (2015) The physics
754 of aeolian sand transport. *C R Phys* 16:1–13
- 755 Virtanen P, Gommers R, Oliphant TE, Haberland M, Reddy T, Cournapeau
756 D, Burovski E, Peterson P, Weckesser W, Bright J, et al. (2020) Scipy 1.0:
757 fundamental algorithms for scientific computing in python. *Nature methods*
758 17:261–272
- 759 Vogelezang D, Holtslag A (1996) Evaluation and model impacts of alternative
760 boundary-layer height formulations. *Boundary-Layer Meteorol* 81:245–269
- 761 Vosper SB (2004) Inversion effects on mountain lee waves. *Q J R Meteorol Soc*
762 130:1723–1748
- 763 Walker I, Davidson-Arnott R, Bauer B, Hesp P, Delgado-Fernandez I, Oller-
764 head J, Smyth T (2017) Scale-dependent perspectives on the geomorphology
765 and evolution of beach-dune systems. *Earth-Science Review* 171:220–253
- 766 Walker IJ, Nickling WG (2002) Dynamics of secondary airflow and sediment
767 transport over and in the lee of transverse dunes. *Prog Phys Geogr* 26(1):47–
768 75
- 769 Walker IJ, Hesp PA, Davidson-Arnott RG, Bauer BO, Namikas SL, Ollerhead
770 J (2009) Responses of three-dimensional flow to variations in the angle of
771 incident wind and profile form of dunes: Greenwich dunes, prince edward
772 island, canada. *Geomorphology* 105:127–138
- 773 Weaver C, Wiggs G (2011) Field measurements of mean and turbulent airflow
774 over a barchan sand dune. *Geomorphology* 128:32–41
- 775 Wiggs G, Bullard J, Garvey B, Castro I (2002) Interactions between airflow
776 and valley topography with implications for aeolian sediment transport.
777 *Physical Geography* 23:366–380

- 778 Zhang C, Li Q, Zhou N, Zhang J, Kang L, Shen Y, Jia W (2016) Field obser-
779 vations of wind profiles and sand fluxes above the windward slope of a sand
780 dune before and after the establishment of semi-buried straw checkerboard
781 barriers. *Aeolian Res* 20:59–70
- 782 Zilker DP, Hanratty TJ (1979) Influence of the amplitude of a solid wavy wall
783 on a turbulent flow. part 2. separated flows. *J Fluid Mech* 90:257–271
- 784 Zilker DP, Cook GW, Hanratty TJ (1977) Influence of the amplitude of a solid
785 wavy wall on a turbulent flow. part 1. non-separated flows. *J Fluid Mech*
786 82:29–51

787 **Local wind regime induced by giant linear dunes**
 788 — Supplementary Material —

789 **C. Gadal* · P. Delorme · C. Narteau · G.F.S. Wiggs · M. Baddock ·**
 790 **J.M. Nield · P. Claudin**

791
 792 * Institut de Mécanique des Fluides de Toulouse, Université de Toulouse Paul
 793 Sabatier, CNRS, Toulouse INP-ENSEEIHT, Toulouse, France.
 794 cyril.gadal@imft.fr

795 **1. Shear velocity and calibration of the hydrodynamical roughness**

796 As the regionally predicted and locally measured velocities are available at
 797 different heights, we can not compare them directly. We therefore convert all
 798 velocities into shear velocities u_* , characteristic of the turbulent velocity profile
 799 (Spalding 1961; Stull 1988):

$$\frac{u(z)}{u_*} = \frac{1}{\kappa} \ln \left(\frac{z}{z_0} \right), \quad (15)$$

800 where z is the vertical coordinate, $\kappa = 0.4$ the von Kármán constant and z_0 the
 801 hydrodynamic roughness. Several measurements of hydrodynamic roughnesses
 802 are available (Raupach 1992; Bauer et al. 1992; Brown et al. 2008; Nield et al.
 803 2014). In the absence of sediment transport, it is governed by the geometric
 804 features of the bed (Flack and Schultz 2010; Pelletier and Field 2016). When
 805 aeolian saltation occurs, it is rather controlled by the altitude of Bagnold's
 806 focal point (Durán et al. 2011; Valance et al. 2015), which depends on the
 807 wind velocity and grain properties (Sherman and Farrell 2008; Zhang et al.
 808 2016; Field and Pelletier 2018). Whether associated with geometric features
 809 or with sediment transport, its typical order of magnitude is the millimetre
 810 scale on sandy surfaces.

811 We do not have precise velocity vertical profiles to be able to deduce an
 812 accurate value of z_0 in the various environments of the meteorological stations
 813 (vegetated, arid, sandy). Our approach is to rather select the hydrodynamic
 814 roughness which allows for the best possible matching between the regionally
 815 predicted and locally measured winds, i.e. minimising the relative difference δ
 816 between the wind vectors of both datasets:

$$\delta = \frac{\sqrt{\langle \|\mathbf{u}_{*,\text{era}} - \mathbf{u}_{*,\text{station}}\|^2 \rangle}}{\sqrt{\langle \|\mathbf{u}_{*,\text{era}}\| \rangle \langle \|\mathbf{u}_{*,\text{station}}\| \rangle}}, \quad (16)$$

817 where $\langle \cdot \rangle$ denotes time average. This parameter is computed for values of z_0
 818 in ERA5-Land analysis ranging from 10^{-5} m to 10^{-2} m for the four different
 819 stations. Note that for the North Sand Sea and South Sand Sea stations, where
 820 the giant dunes feedback presumably affect the wind, we take into account the
 821 non-deflected winds only in the calculation of δ (with a 15° tolerance).

As shown in Online Resource Fig. S4, the minimum values of δ in the space $(z_0^{\text{ERA5Land}}, z_0^{\text{local}})$ form a line. We thus set the roughness in the ERA5-Land analysis to the typical value $z_0 = 10^{-3}$ m, and deduce the corresponding ones for the local stations. It leads to 2.7, 0.8, 0.1 and 0.5 mm for the Etosha West, North Sand Sea, Huab and South Sand Sea stations, respectively. Importantly, this approach somewhat impacts the calculation of the shear velocities, but not that of the wind directions. As such, most of our conclusions are independent of such a choice. However, it may affect the magnitude of the wind velocity attenuation/amplification in flow confinement situations.

2. Computation of the ABL characteristics

The estimation of the non-dimensional numbers associated with the ABL requires the computation of representative meteorological quantities. In arid areas, the vertical structure of the atmosphere can be approximated by a well mixed convective boundary layer of height H , topped by the stratified free atmosphere (Stull 1988; Shao 2008). In this context, one usually introduces the virtual potential temperature T_{vp} , which is a constant T_0 inside the boundary layer, and increases linearly in the FA (Online Resource Fig. S12a):

$$T_{\text{vp}}(z) = \begin{cases} T_0 & \text{for } z \leq H, \\ T_0 \left(1 + \frac{\Delta T_{\text{vp}}}{T_0} + \frac{N^2}{g}(z - H) \right) & \text{for } z \geq H, \end{cases} \quad (17)$$

where ΔT_{vp} is the temperature discontinuity at the capping layer and $N = \sqrt{g\partial_z T_{\text{vp}}/T_0}$ is the Brunt-Väisälä frequency, characteristic of the stratification. Note that, under the usual Boussinesq approximation, temperature and air density variations are simply related by $\delta T_{\text{vp}}/T_0 \simeq -\delta\rho/\rho_0$ (see Online Resource of Andreotti et al. (2009)), so that N can equivalently be defined from the density gradient as next to Eq. 1.

The ERA5 dataset provides vertical profiles of the geopotential ϕ , the actual temperature T and the specific humidity η at given pressure levels P . The vertical coordinate is then calculated as:

$$z = \frac{\phi R_t}{g R_t - \phi}, \quad (18)$$

where $R_t = 6371229$ m is the reference Earth radius and $g = 9.81$ m s⁻² is the gravitational acceleration. One also computes the virtual potential temperature as:

$$T_{\text{vp}} = T \left[1 + \left(\frac{M_d}{M_w} - 1 \right) \eta \right] \left(\frac{P_0}{P} \right)^{R/C_p}, \quad (19)$$

where $P_0 = 10^5$ Pa is the standard pressure, $R = 8.31$ J/K is the ideal gas constant, $C_p \simeq 29.1$ J/K is the air molar heat capacity, and $M_w = 0.018$ kg/Mol

853 and $M_d = 0.029 \text{ kg/Mol}$ are the molecular masses of water and dry air respectively.
 854 The specific humidity is related to the vapour pressure p_w as

$$\eta = \frac{\frac{M_w}{M_d} p_w}{p - \left(1 - \frac{M_w}{M_d}\right) p_w}. \quad (20)$$

855 The ERA5 dataset also provides an estimate of the ABL depth H , based
 856 on the behaviour of the Richardson vertical profile. This dimensionless num-
 857 ber is defined as the ratio of buoyancy and flow shear terms, and can be
 858 expressed as $\text{Ri} = N^2 / (\partial_z u)^2$. It vanishes in the lower well-mixed layer where
 859 T_{vp} is constant, and increases in the stratified FA. Following the method and
 860 calibration of Vogelegang and Holtslag (1996); Seidel et al. (2012), the value
 861 $\text{Ri}(z) \simeq 0.25$ has been shown to be a good empirical criterion to give $z \simeq H$
 862 within a precision varying from 50% for the shallower ABL (e.g. at night) to
 863 20% for situations of stronger convection.

864 Examples of vertical profiles of the virtual potential temperature deduced
 865 from ERA5 are shown in Online Resource Fig. S12a. For each of them, an
 866 average temperature is computed below the ABL depth ($z < H$), and a linear
 867 function is fitted above, allowing us to extract the temperature jump ΔT_{vp} .
 868 Importantly, some profiles display a vertical structure that cannot be approx-
 869 imated by the simple form (17) used here (Online Resource Fig. S12b). In
 870 practice, we removed from the analysis all of those leading to the unphysical
 871 case $\Delta T_{\text{vp}} < 0$. We have noticed that these ‘ill-processed’ profiles dominantly
 872 occur in winter and are evenly spread across the hours of the day. Importantly,
 873 they represent $\simeq 12\%$ of the data only (Online Resource Fig. S12c,d), and we
 874 are thus confident that this data treatment does not affect our conclusions.

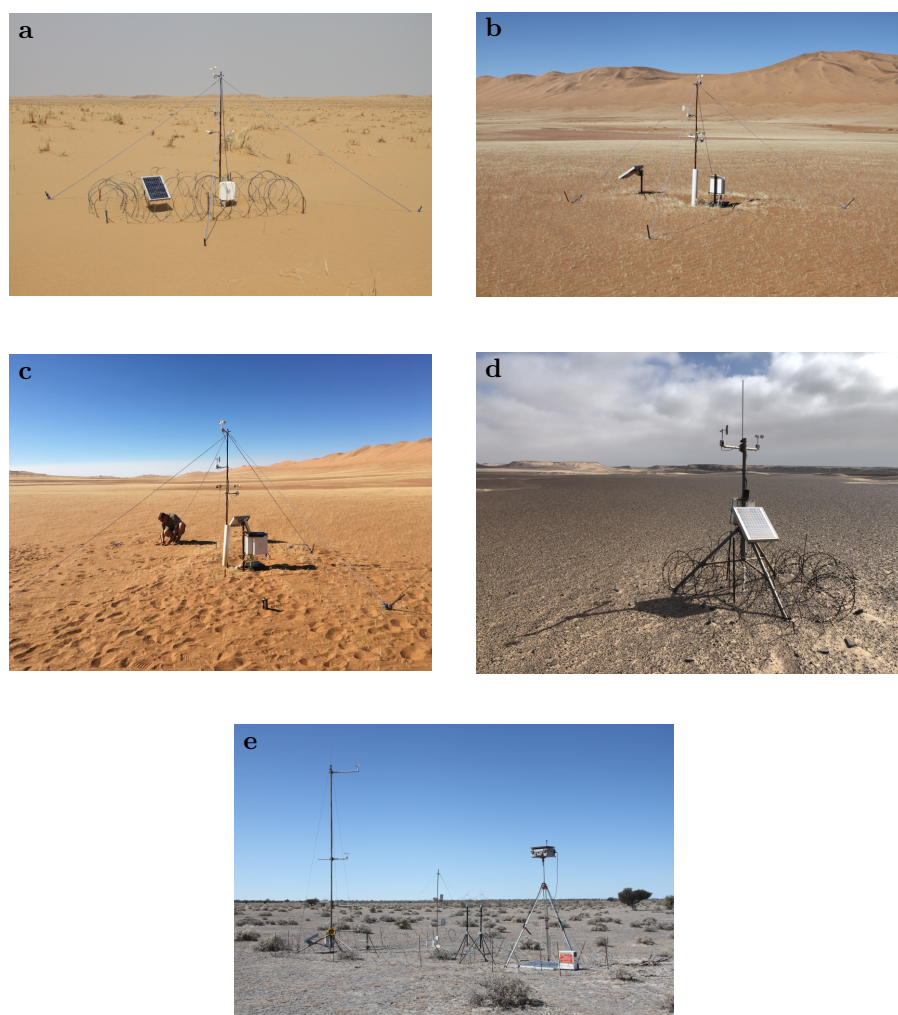


Fig. S1 Photographs of the meteorological stations. **a:** South Sand Sea station. **b–c:** North Sand Sea station. **d:** Huab station. **e:** Etosha West station.

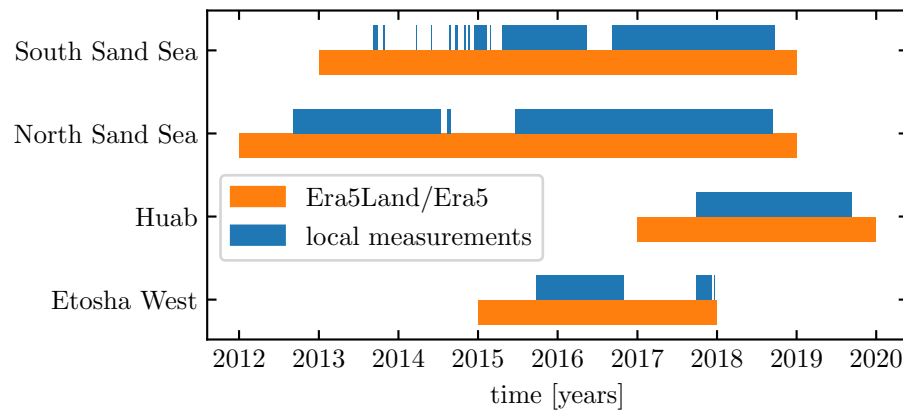


Fig. S2 Gant chart representing the valid time steps for the two data sets, for all stations.

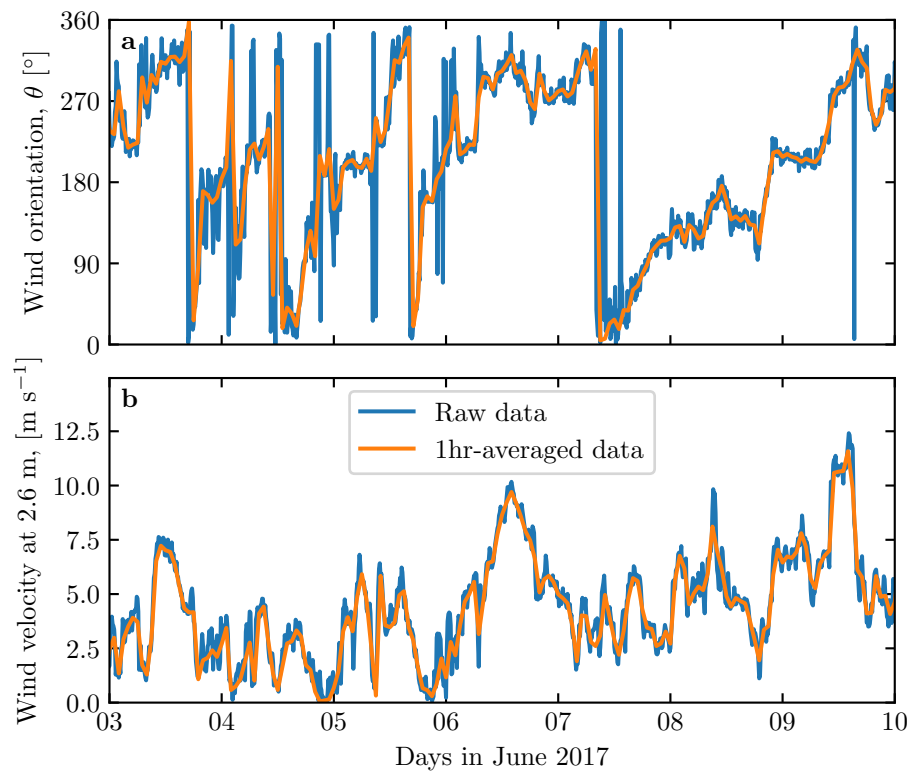


Fig. S3 Comparison between raw local wind measurements, and hourly-averaged data for South Sand Sea station. **a:** wind direction. **b:** wind velocity at height 2.6 m.

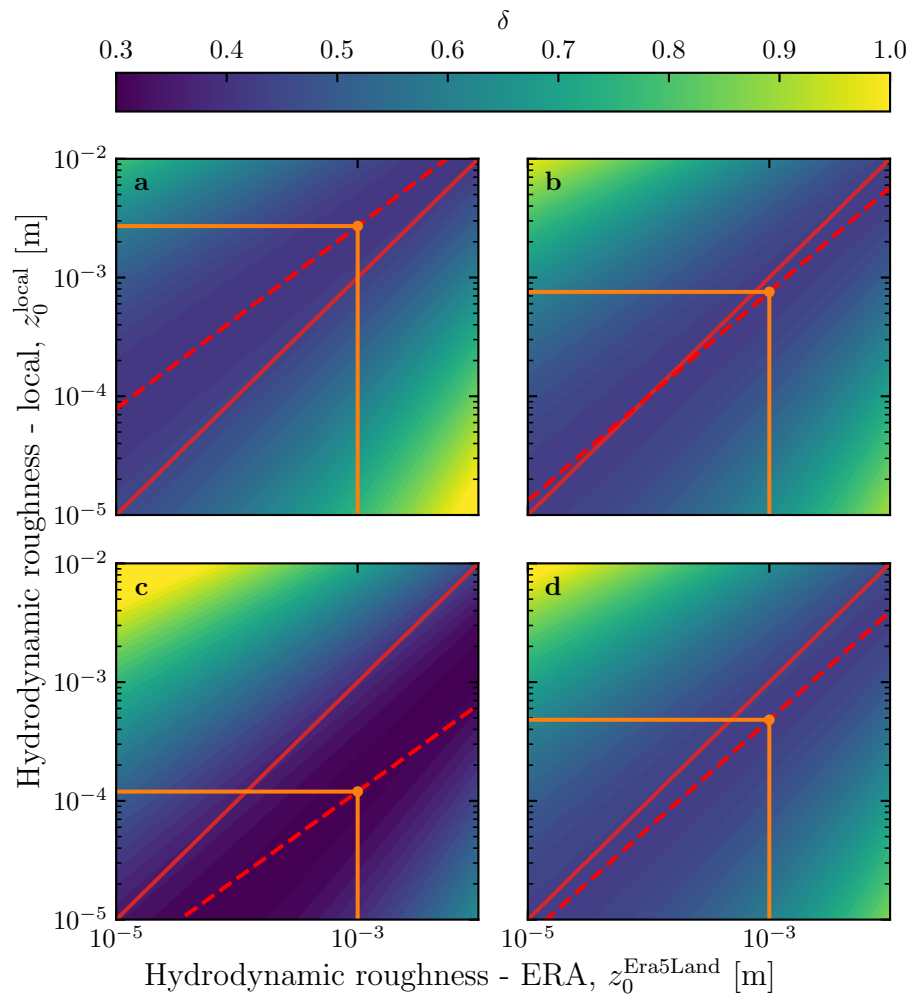


Fig. S4 Calibration of hydrodynamic roughness. The parameter δ (Eq. 16) quantifying the difference between local and predicted winds is shown in colorscale as a function of the hydrodynamic roughnesses chosen for the ERA5-Land and for local winds, for the (a) Etosha West, (b) North Sand Sea, (c) Huab and (d) South Sand Sea stations. The red dashed and plain lines shows the minima of δ and the identity line, respectively. The orange lines and dots highlight the chosen hydrodynamic roughnesses for the local winds deduced from setting $z_0^{\text{ERA5Land}} = 1 \text{ mm}$.

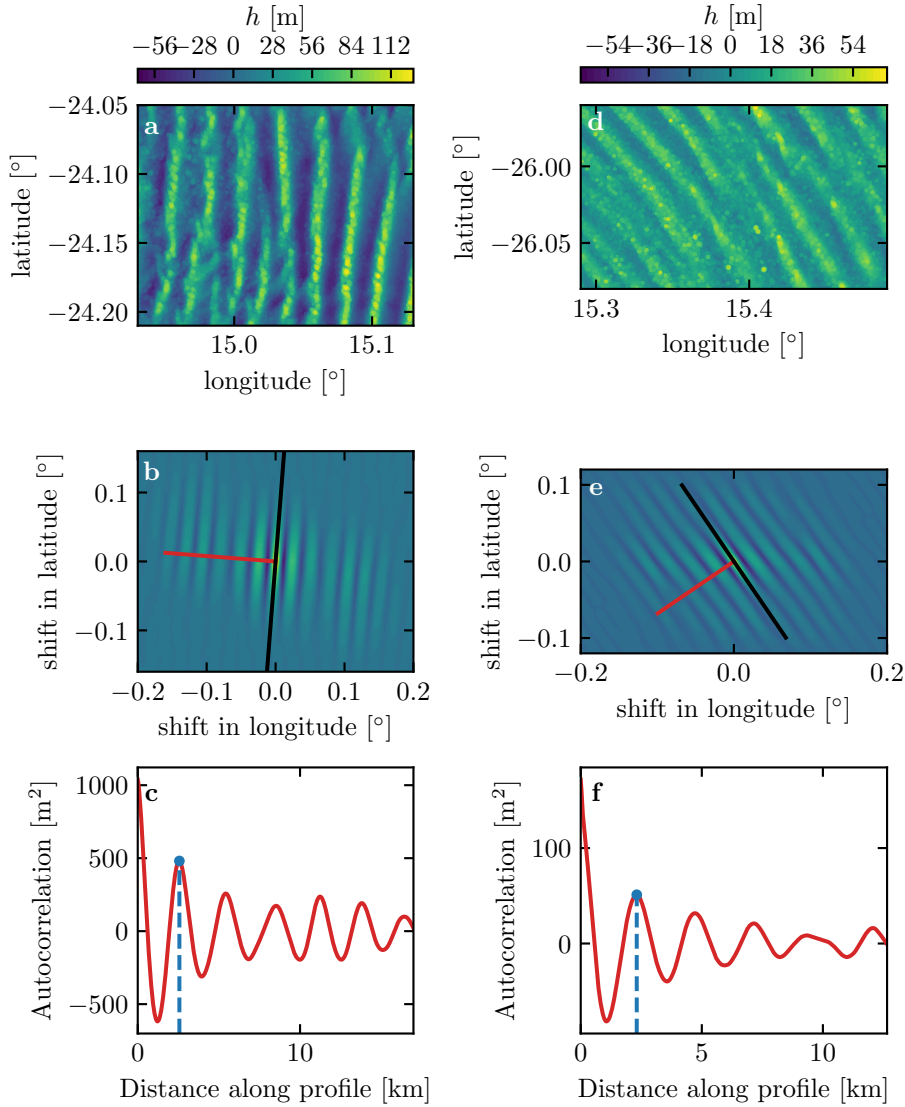


Fig. S5 Analysis of the DEMs of the North Sand Sea (left column – panels **a**, **b**, **c**) and South Sand Sea (right column – panels **d**, **e**, **f**) stations. **a–d**: Bed elevation detrended by a fitted second order polynomial base-line. **b–e**: Autocorrelation matrix shown in colorscale. The black line shows the detected dune orientation, and the red line represents the autocorrelation profile along which the dune wavelength is calculated, displayed in **c–f**. The blue lines and dots show the first peak of the autocorrelation profile, whose abscissa gives the characteristic wavelength of the dune pattern.

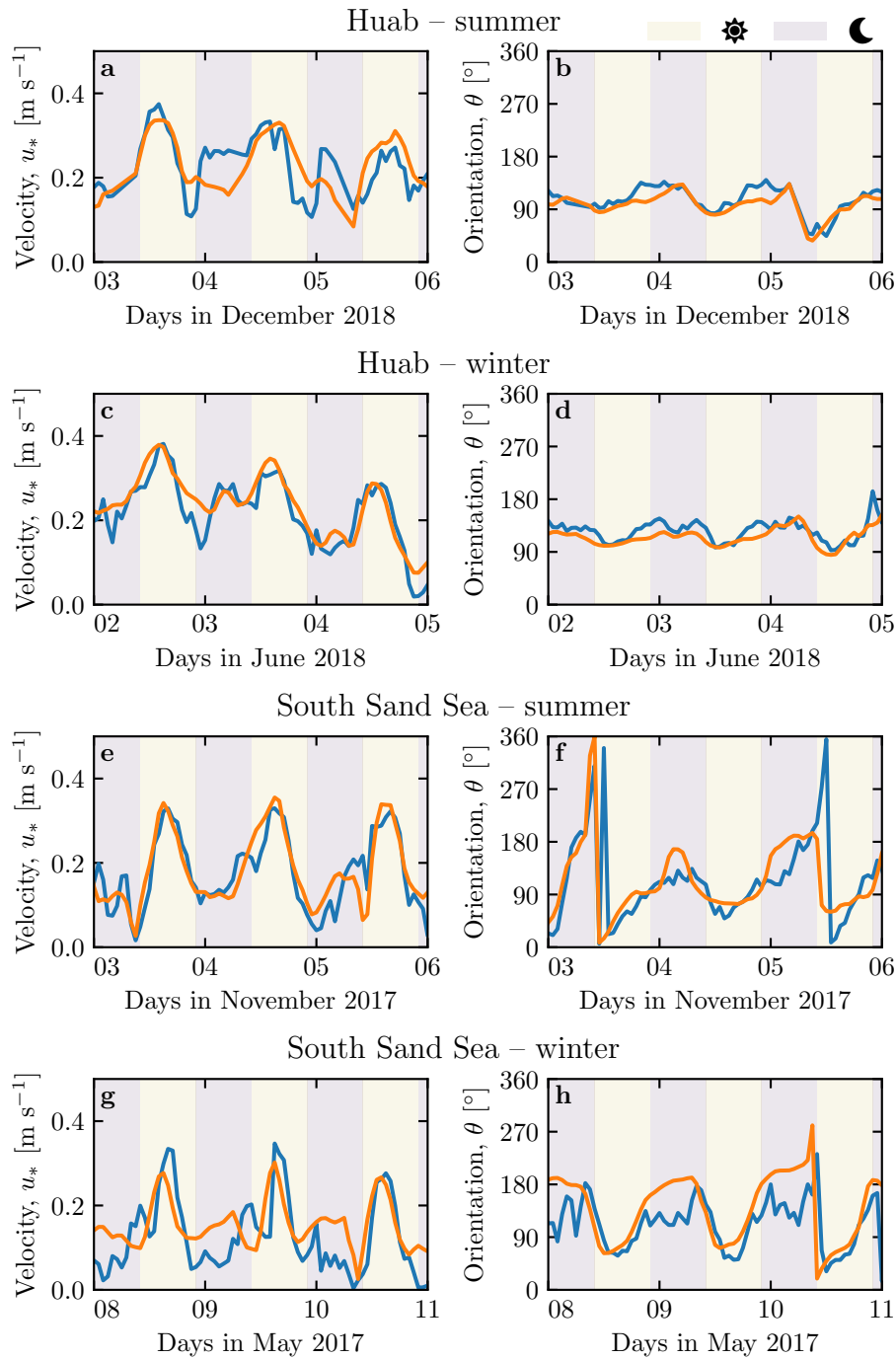


Fig. S6 Temporal comparison between the wind data coming from the ERA5-Land climate reanalysis (orange lines) and from the local measurements (blue lines). Coloured swathes indicate day (between 1000 UTC and 2200 UTC) and night (before 1000 UTC or after 2200 UTC) **a–b**: Huab station in summer. **b–c**: Huab station in winter. **d–e**: South Sand Sea station in summer. **f–g**: South Sand Sea station in winter.

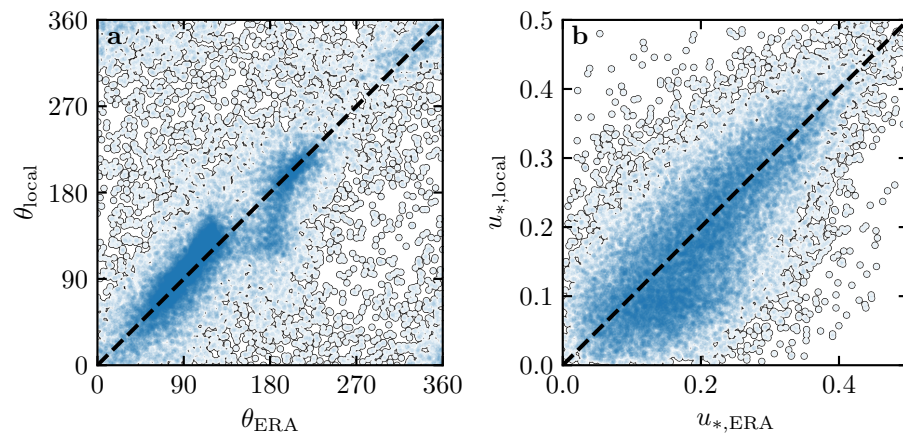


Fig. S7 Statistical comparison of the wind orientation (a) and velocity (b) between the ERA5-Land dataset and the local measurements for the Huab and Etosha West stations. Data point clustering around identity lines (dashed and black) provide evidence for agreement of the two sets.

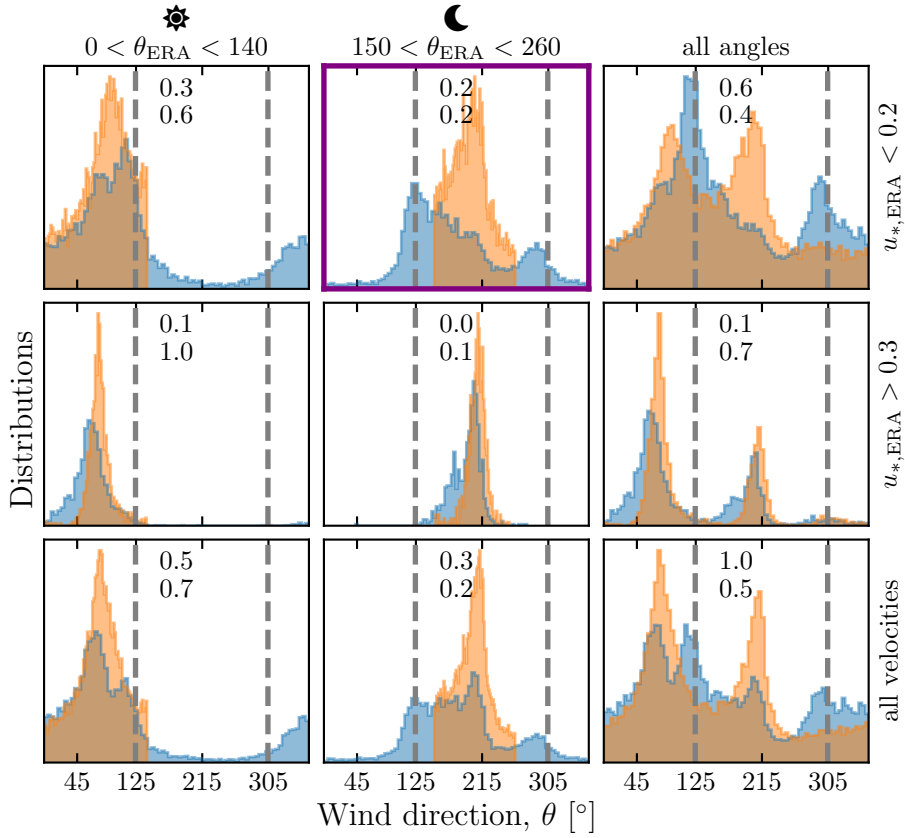


Fig. S8 Distributions of wind direction at the South Sand Sea Station for the ERA5-Land climate reanalysis (orange) and the local measurements (blue) – equivalent of Fig. 3. In each subplot, both distributions are plotted from the same time steps, selected with constraints on the wind direction (columns) and/or wind velocity (rows) in the ERA5-Land dataset. The gray vertical dashed lines indicate the dune orientation. The numbers at the top centre give the percentage of time steps selected in each sub-range, as well as the percentage of them corresponding to the day (between 1000 UTC and 2200 UTC). The purple frame highlights the regime (small wind velocities, nocturnal summer wind) during which the wind data from both datasets differ.

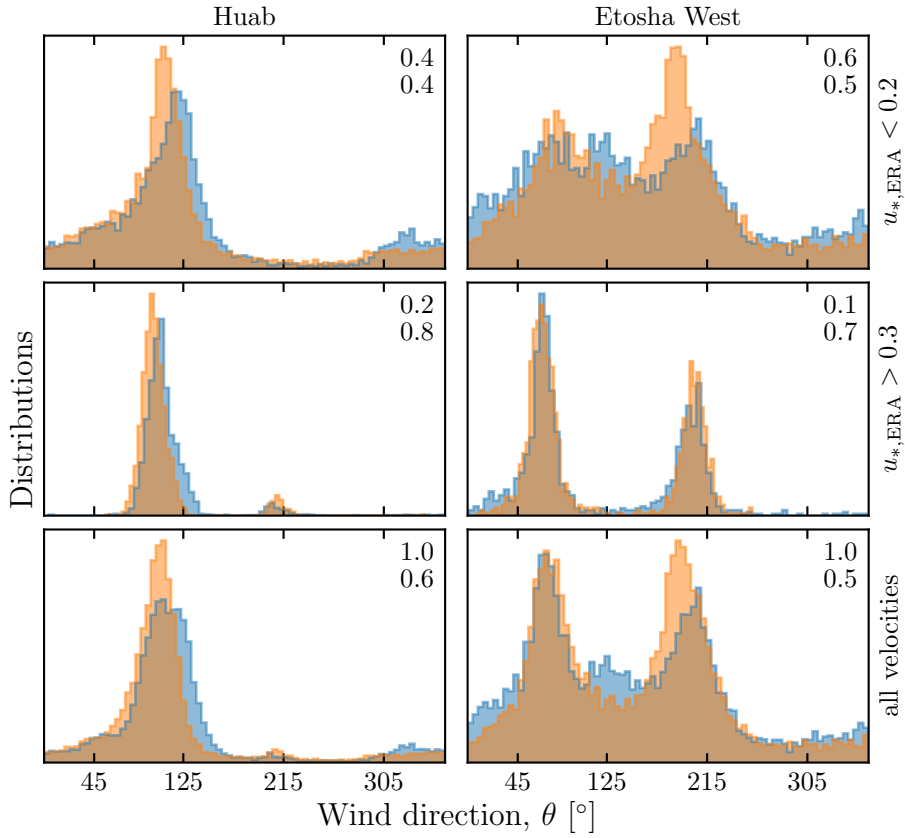


Fig. S9 Distributions of wind direction at the Huab and Etosha West stations for the ERA5-Land climate reanalysis (orange) and the local measurements (blue). In each subplot, both distributions are plotted from the same time steps, selected with constraints on the wind wind velocity (rows) in the ERA5-Land dataset. The numbers at the top centre give the percentage of time steps selected in each sub-range, as well as the percentage of them corresponding to the day (between 1000 UTC and 2200 UTC). Compared to the North and South Namib stations (Fig. 3 and Fig. S8), histograms match for high and low velocities.

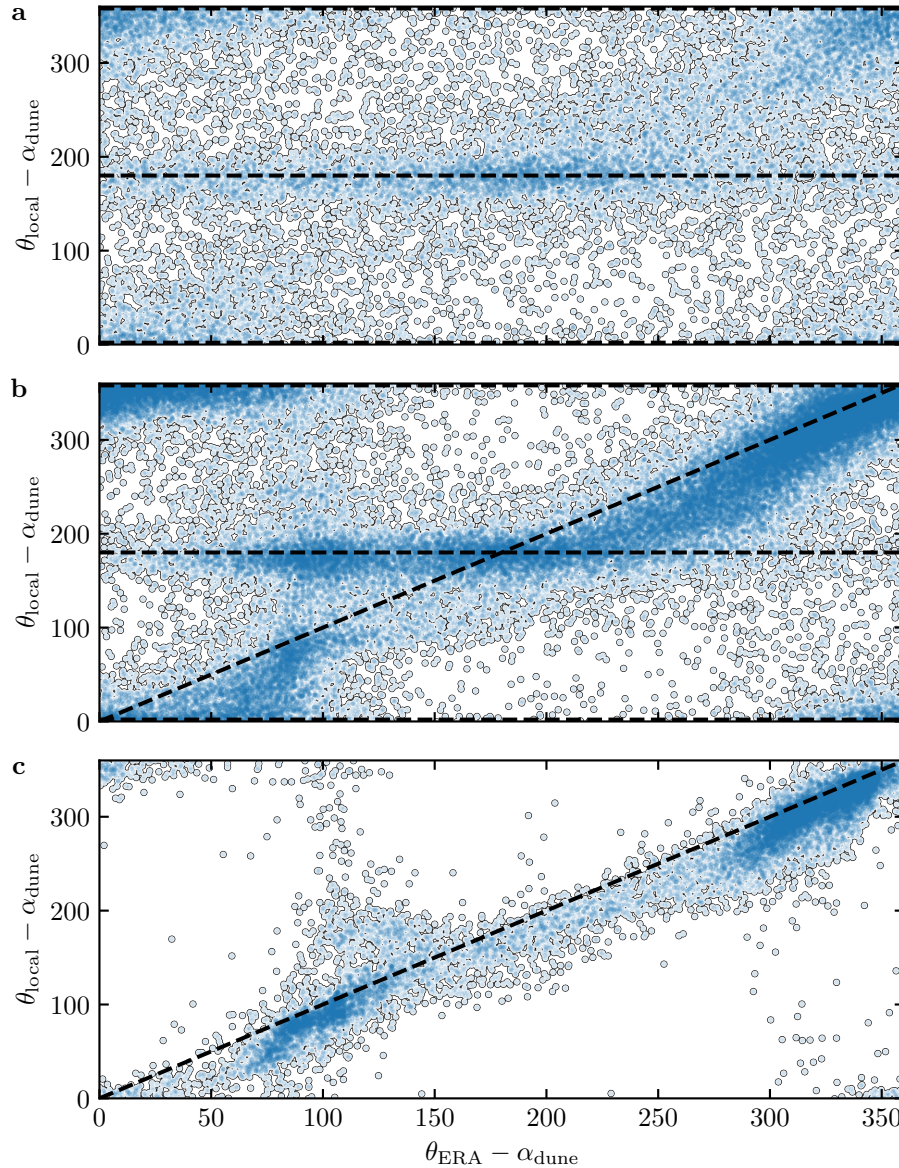


Fig. S10 Statistical comparison of the wind orientation between the ERA5-Land dataset and the local measurements for the South Sand Sea and North Sand Sea stations, for different velocity ranges. **a:** $u_{*,\text{ERA}} < 0.1 \text{ m s}^{-1}$. **b:** $0.1 < u_{*,\text{ERA}} \leq 0.25 \text{ m s}^{-1}$. **c:** $u_{*,\text{ERA}} \geq 0.25 \text{ m s}^{-1}$. The measured dune orientations are subtracted to the wind orientation, which allows us to plot both stations on the same graph. Black dashed lines indicate locally measured orientations aligned with the dune crests (here 0°, 180° and 360° – panels a, b), as well as the identity lines (panels b, c).

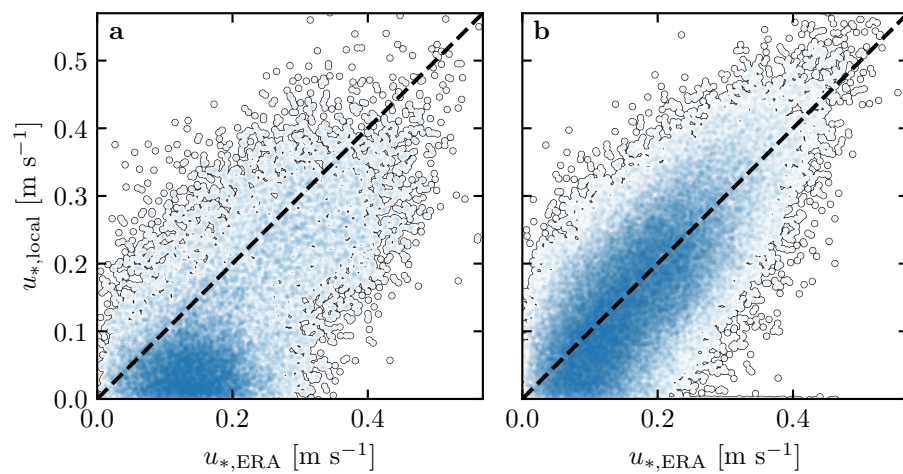


Fig. S11 Statistical comparison of the wind velocity between the ERA5-Land dataset and the local measurements for the South Sand Sea and North Sand Sea stations. **a:** Nocturnal summer easterly wind. **b:** Diurnal southerly wind. Black dashed lines are identity lines. The angle ranges used to select diurnal and nocturnal summer winds are the same as those in Fig. 3 and Online Resource Fig. S8.

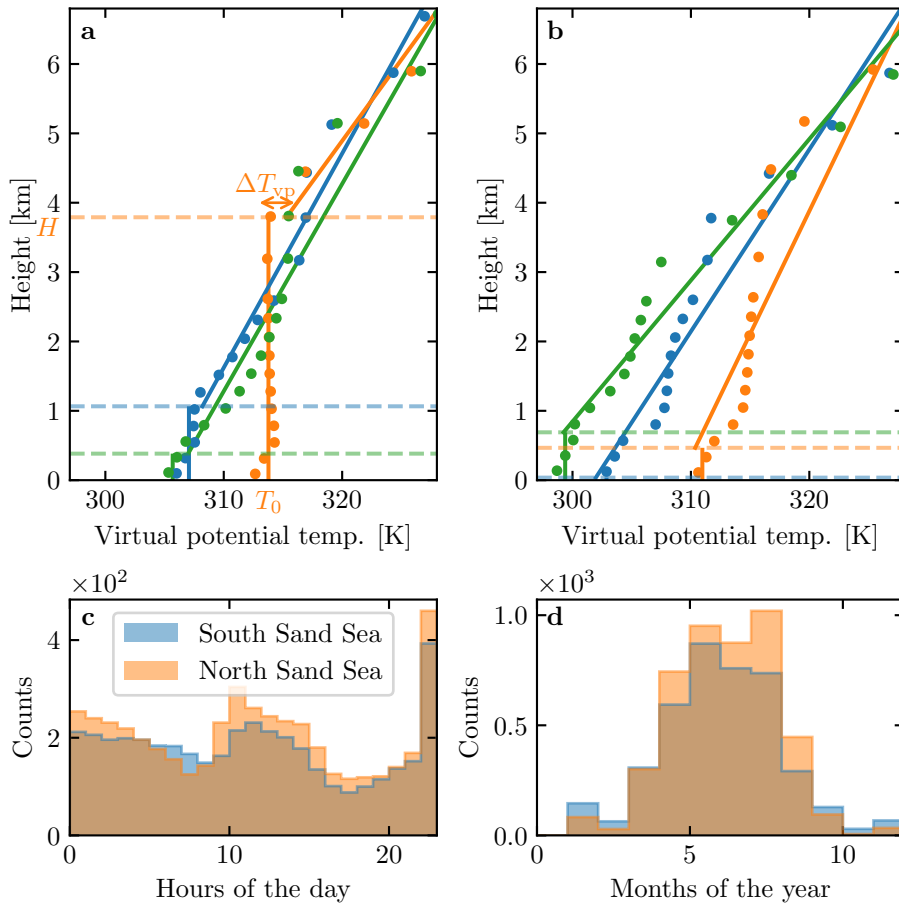


Fig. S12 **a:** Vertical profiles of the virtual potential temperature at three different times (blue: 29/11/2012 - 1100 UTC, orange: 21/03/2017 - 1200 UTC, green: 21/03/2017 - 2000 UTC) at the South Sand Sea station. Dots: data from the ERA5 reanalysis. Dashed lines: boundary layer height given by the ERA5 reanalysis. Plain lines: vertical (ABL) and linear (FA) fits to estimate the quantities displayed in Online Resource Fig. S13. **b:** Examples of ill-processed vertical profiles at three different times (blue: 2/12/2013 - 2300 UTC, orange: 20/03/2017 - 0000 UTC, green: 14/07/2017 - 1400 UTC) at the South Sand Sea station. **c:** Hourly distribution of ill-processed vertical profiles. **d:** Monthly distribution of ill-processed vertical profiles.

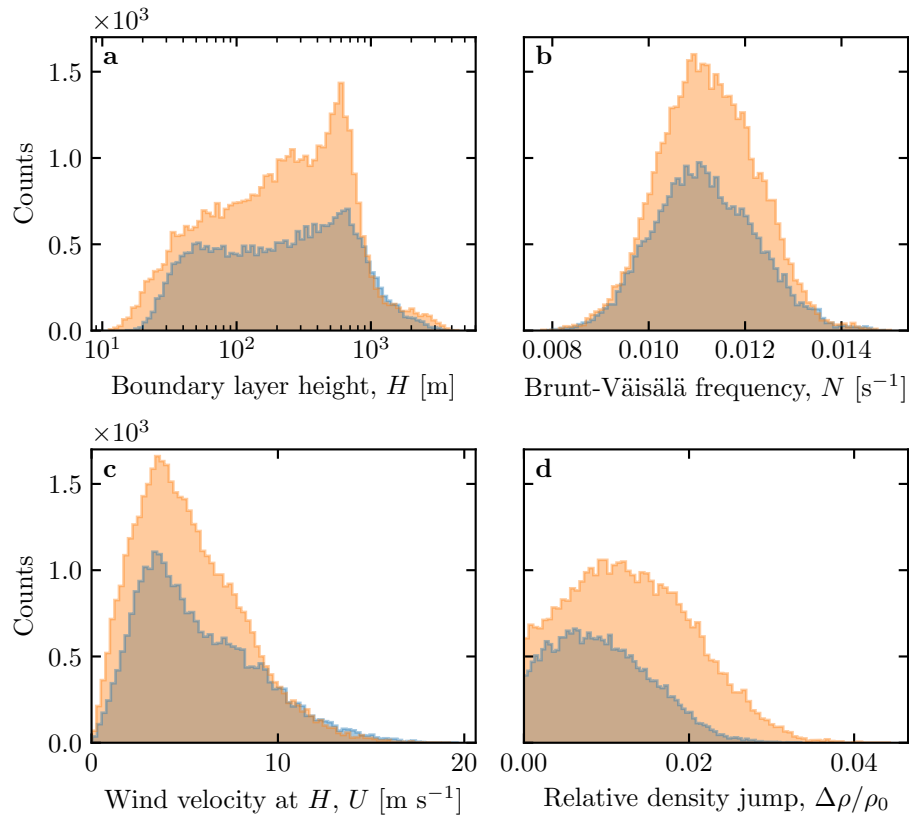


Fig. S13 Distributions of the meteorological parameters resulting from the processing of the ERA5-Land data for the South Sand Sea (blue) and the North Sand Sea (orange) stations.

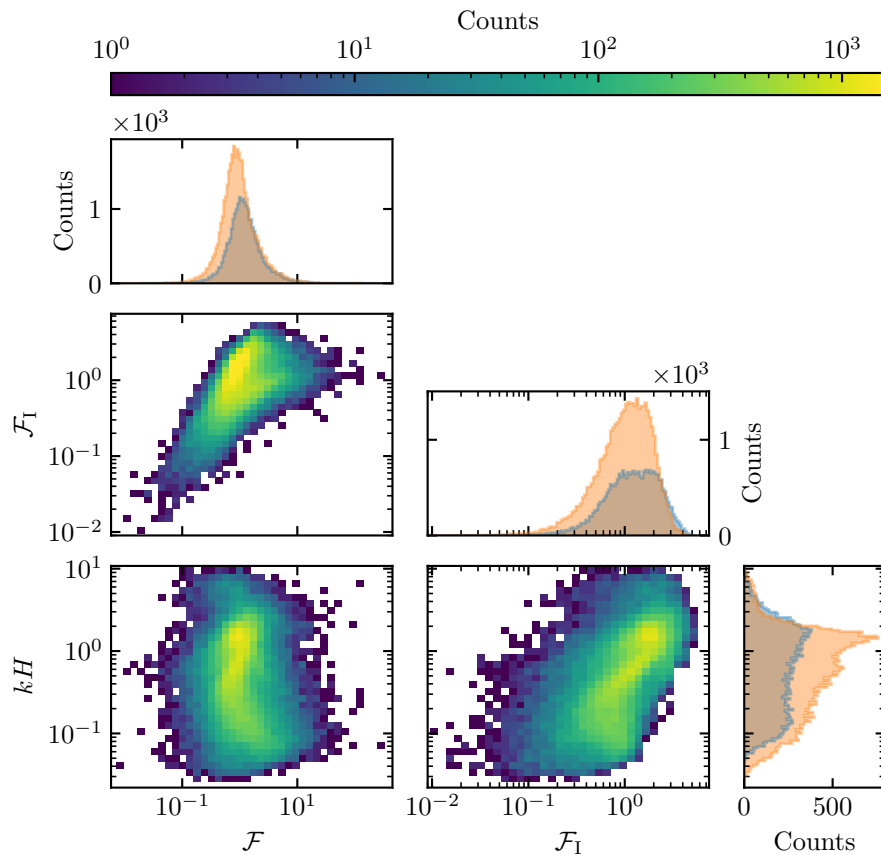


Fig. S14 Non-dimensional parameters distributions. For the marginal distributions, the orange correspond to the South Sand Sea station, and the blue to the North Sand Sea station.

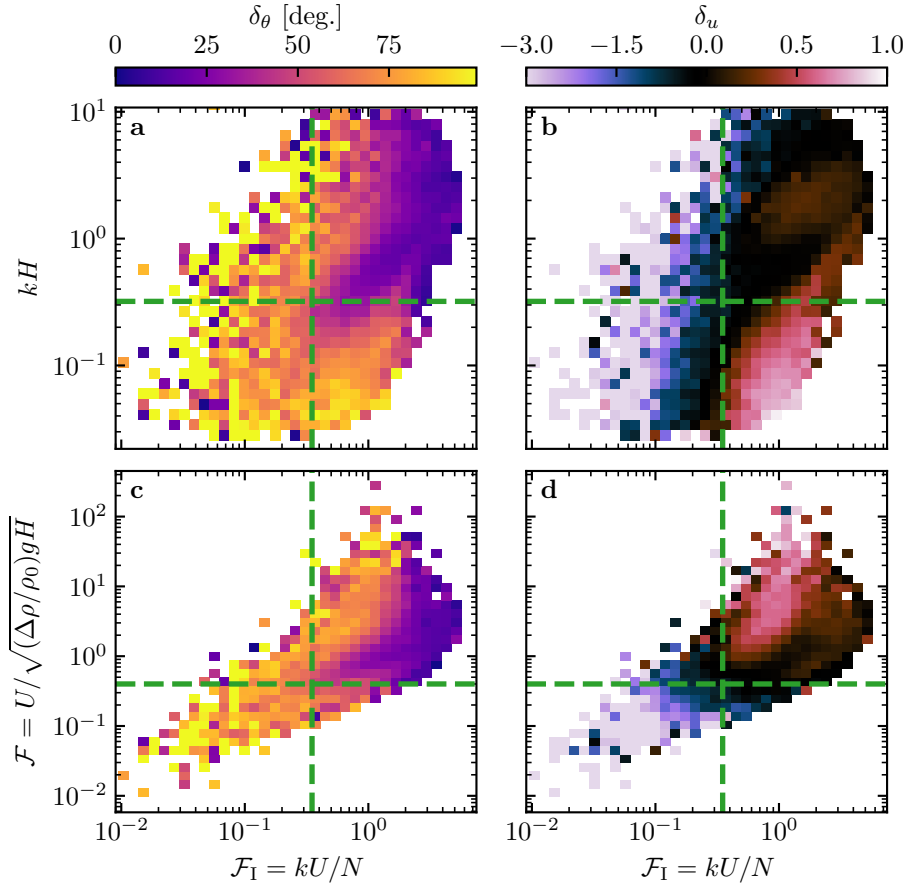


Fig. S15 Regime diagrams of the wind deviation δ_θ and relative attenuation/amplification δ_u in the spaces (\mathcal{F}_I, kH) and $(\mathcal{F}_I, \mathcal{F})$, containing the data from both the North Sand Sea and South Sand Sea stations. Green dashed lines empirically delimit the different regimes. The point density in each bin of the diagrams is shown in Online Resource Fig. S14 – 95% of the data occur in the range $-1 < \delta u < 1$. The similar regime diagrams in the space (\mathcal{F}, kH) are shown in Fig. 5.

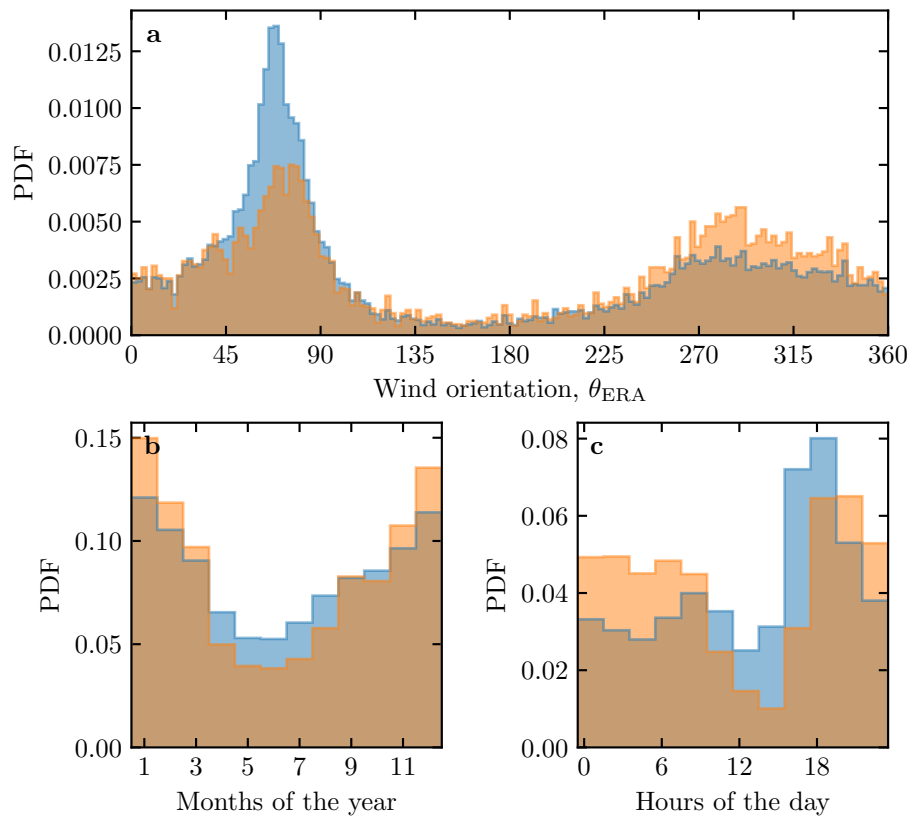


Fig. S16 Normalized distributions of amplified velocities for the North sand Sea (blue: $\delta_u < 0$, orange: $\delta_u < -0.5$). **a:** Angular distributions. **b:** Monthly distributions. **c:** Hourly distributions.

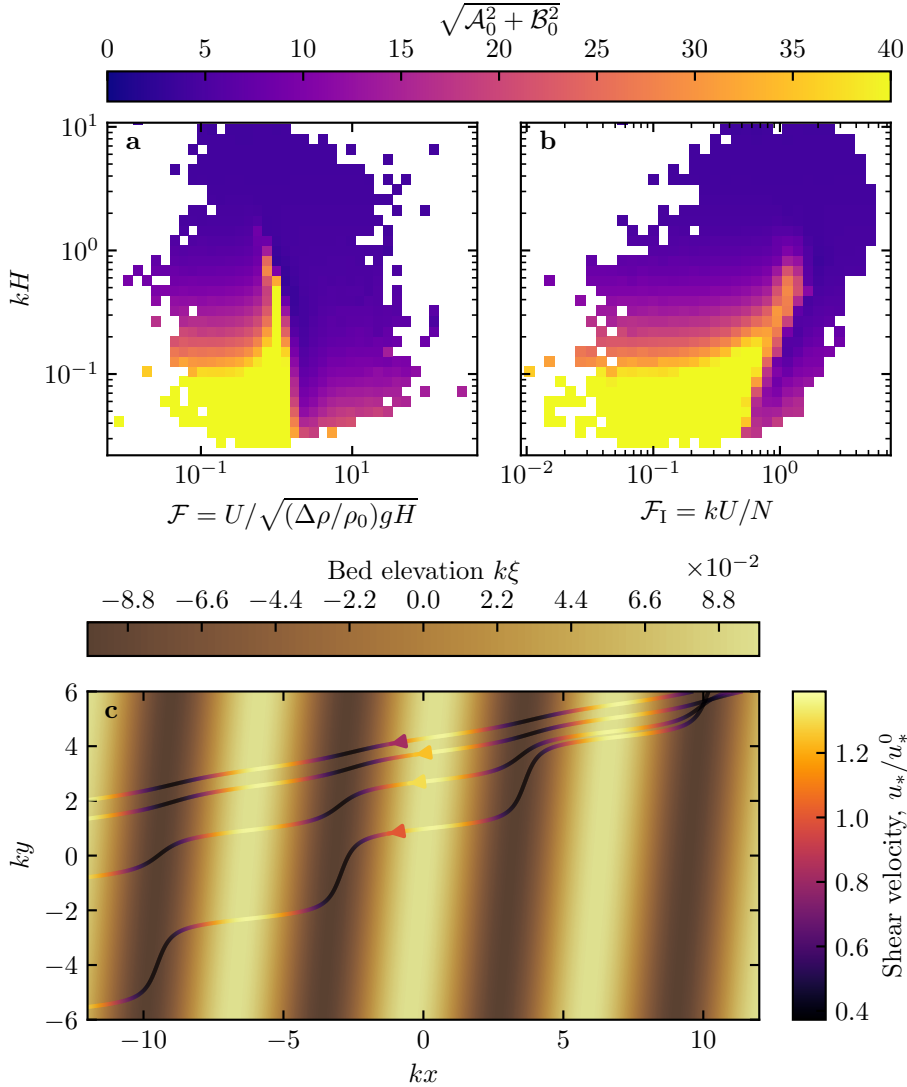


Fig. S17 Computation of the flow disturbance with the linear model of Andreotti et al. (2009). **a** and **b** Magnitude of the hydrodynamic coefficients A_0 and B_0 , calculated from the values of the non-dimensional numbers corresponding to the ERA5-Land time series presented in Figs. 4 and 5. **c** Shear velocity streamlines over sinusoidal ridges of amplitude $k\xi_0 = 0.1$ and for increasing values of $\sqrt{A_0^2 + B_0^2}$. From the upper to the lower streamline, values of $(kH, \mathcal{F}, \mathcal{F}_I, A_0, B_0, \sqrt{A_0^2 + B_0^2})$ are $(1.9, 0.6, 1.5, 3.4, 1.0, 3.5)$, $(1.5, 0.3, 0.4, 4.8, 1.4, 5.0)$, $(0.1, 3.5, 1.0, 8.6, 0.1, 8.6)$, $(0.5, 0.05, 0.04, 9.6, 2.5, 9.9)$.